Degeneration of internal Kelvin waves in a continuous two-layer stratification

Hugo N. Ulloa[1,†], Kraig B. Winters[2], Alberto de la Fuente[1] and Yarko Niño[1,3]

[1]Departamento de Ingeniera Civil, Universidad de Chile, Av. Blanco Encalada 2002, CP 8370449, Santiago, Chile

[2]Scripps Institution of Oceanography and Mechanical and Aerospace Engineering, University of California San Diego, La Jolla, CA 92093, USA

[3]Advanced Mining Technology Center, Universidad de Chile, Av. Tupper 2007, CP 8370451, Santiago, Chile

We explore the evolution of the gravest internal Kelvin wave in a two-layer rotating cylindrical basin, using direct numerical simulations (DNS) with a hyper-viscosity/diffusion approach to illustrate different dynamic and energetic regimes. The initial condition is derived from Csanady's (*J. Geophys. Res.*, vol. 72, 1967, pp. 4151–4162) conceptual model, which is adapted by allowing molecular diffusion to smooth the discontinuous idealized solution over a transition scale, δ_i, taken to be small compared to both layer thicknesses h_ℓ, $\ell = 1, 2$. The different regimes are obtained by varying the initial wave amplitude, η_0, for the same stratification and rotation. Increasing η_0 increases both the tendency for wave steepening and the shear in the vicinity of the density interface. We present results across several regimes: from the damped, linear–laminar regime (DLR), for which $\eta_0 \sim \delta_i$ and the Kelvin wave retains its linear character, to the nonlinear–turbulent transition regime (TR), for which the amplitude η_0 approaches the thickness of the (thinner) upper layer h_1, and nonlinearity and dispersion become significant, leading to hydrodynamic instabilities at the interface. In the TR, localized turbulent patches are produced by Kelvin wave breaking, i.e. shear and convective instabilities that occur at the front and tail of energetic waves within an internal Rossby radius of deformation from the boundary. The mixing and dissipation associated with the patches are characterized in terms of dimensionless turbulence intensity parameters that quantify the locally elevated dissipation rates of kinetic energy and buoyancy variance.

Key words: stratified flows, transition to turbulence, waves in rotating fluids

1. Introduction

Physical processes that control the degeneration of basin-scale internal gravity waves (IGW) in stratified lakes affected by earth's rotation have been subject of considerable interest for several decades, owing to their impact on transport and water quality (Wüest & Lorke 2003; Boehrer & Schultze 2008). In these aquatic systems,

† Email address for correspondence: hulloa@ing.uchile.cl

the fundamental IGWs are the known Poincaré and Kelvin waves (Lamb 1932; Csanady 1967), where the latter IGW is usually the most energetic mode (Antenucci & Imberger 2001; Stocker & Imberger 2003). Field measurements have shown that the passage of internal Kelvin waves (IKWs) is correlated with high-frequency internal waves (Boegman *et al.* 2003; Lorke, Peeters & Bäuerle 2006; de la Fuente *et al.* 2010), shear instabilities and local overturns near the wave troughs in the near-shore regions (Preusse, Peeters & Lorke 2010; Preusse, Freistühler & Peeters 2012*a*). These processes lead to significant localized turbulence and mixing in the pelagic thermocline (Lorke 2007; Bouffard & Lemmin 2013). Over the course of the stratified season, dynamical changes in the wave regime can alter the spatial and temporal distribution of turbulent activity induced by Kelvin waves.

Previous numerical and laboratory studies have analysed the IKW evolution in laminar and weakly nonlinear regimes, obtaining that the wave amplitude, stratification and rotation play an important role in the degeneration and damping processes (de la Fuente *et al.* 2008; Shimizu & Imberger 2009; Sakai & Redekopp 2010; Rozas *et al.* 2014; Ulloa, de la Fuente & Niño 2014). Here we extend the study of the IKWs to nonlinear regimes at which turbulence starts to emerge, using continuous and smooth solutions that allow control the wavefront steepening and the interfacial shear flow through the initial wave amplitude.

In this study we analyse the degeneration of the 'gravest internal Kelvin wave' (hereinafter IKW) in a two-layer stratified basin under different dynamic regimes; from a laminar, linear flow to a nonlinear regime characterized by the transition to turbulence. To this end, we have performed three-dimensional direct numerical simulations (DNS) of the governing equations in a cylindrical domain. The governing equations are the standard three-dimensional Boussinesq equations with *m*-order hyper-viscosity/diffusion operators (Winters & D'Asaro 1997; Waite & Bartello 2004). The use of a hyper-viscosity/diffusion approach enabled us to increase the scale separation between the forcing and dissipation length scales, producing a larger inertial subrange in the model while confining the dissipation length scales as close as possible to the grid spacing (Spyksma, Magcalas & Campbell 2012). The use of a cylindrical domain permits the derivation of the linear modal structure of IKWs for a discontinuous two-layer stratification (Csanady 1967). This solution was then allowed to diffuse vertically via Laplacian diffusion and molecular diffusivities for mass and momentum for a finite time interval producing slightly smoothed versions of linear normal modes in a continuous, nearly two-layer stratification. The length scale δ_i defines the thickness of the sharp pycnocline, which is constrained to be smaller than the thinner upper layer thickness h_1. The advantage of this approach is twofold. First, continuous representations of the model solutions are required for the initialization of the numerical model. Second, in calculating the modal solutions, the amplitude of the interface displacement can be taken as a significant fraction of the upper layer thickness without introducing density overturns, whereas if the equations are first linearized about a smooth but sharp density interface, modal amplitudes are restricted to values significantly smaller than the interface scale δ_i.

Figure 1 shows a schematic of the conceptual model, where the subscripts 1 and 2 indicate the upper and lower layer, respectively. The horizontal and vertical length scales are the diameter D, equal to twice the radius R, and the sum of the two layer thicknesses $H = h_1 + h_2$, respectively; ρ_ℓ denotes the density of the ℓth layer. Rotation is characterized by the inertial frequency f, which, together with the linear internal celerity, $c_i = \sqrt{g'h_1h_2/H}$, define the internal Rossby radius of deformation, $R_i = c_i/f$, from the boundary to the interior, where $g' = g\Delta\rho/\rho_1$ is the reduced gravity and
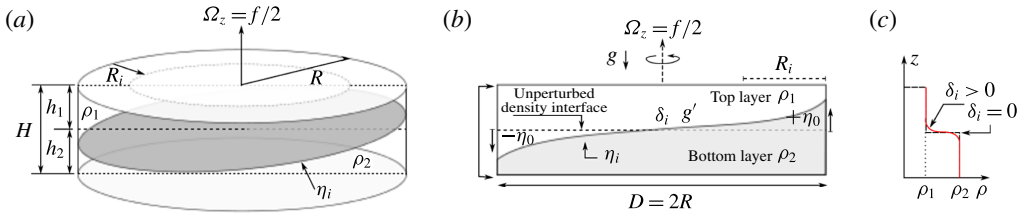
FIGURE 1. (Colour online) Schematic of the conceptual model. (*a*) Three-dimensional view of the domain, a two-layer rotating cylindrical basin of radius R and total depth H. (*b*) Two-dimensional plane across a diameter of the basin. (*c*) Vertical density profile at the centre of the basin (the continuous line denotes a smooth two-layer stratification).

$\Delta\rho = \rho_2 - \rho_1$. The vertical displacement of the density interface is defined as η_i, whose maximum initial amplitude is hereinafter denoted by $\eta_0 = \max\{\eta_i(t = 0, \boldsymbol{x})\}$. Note that because of the spatial structure of IKWs, η_0 occurs at the shoreline (Csanady 1967), i.e. near the vertical sidewalls in our experiments. Our experiments consist of initializing the flow with instantaneous snapshots of smoothed IKW modal solutions at various initial amplitudes η_0 and allowing these initial conditions to evolve under the nonlinear, non-hydrostatic equation of motion.

The outline of the paper is as follows. In §2 we introduce the equations of motion, dimensionless parameters and the set of numerical experiments. In §3 the IKW response is described in terms of dynamic regimes, while in §4 we analyse the spatiotemporal distribution of the turbulent activity, focusing on those IKWs in the laminar–turbulent transition regime. Finally, we summarize and discuss our results in §5.

2. Formulation

2.1. *Governing equations and boundary conditions*

We study the IKW flow via the numerical solution of the Boussinesq equations of motion for a rotating stratified fluid on an f-plane with a m-order viscosity/diffusion operator, written as

$$\frac{\mathrm{D}\boldsymbol{v}}{\mathrm{D}t} + (f\hat{\boldsymbol{k}}) \times \boldsymbol{v} + \frac{\rho}{\rho_0}g\hat{\boldsymbol{k}} = -\frac{1}{\rho_0}\boldsymbol{\nabla}p + \mathcal{D}_m(\boldsymbol{v}), \quad \frac{\mathrm{D}\rho}{\mathrm{D}t} = \mathcal{D}_m(\rho), \ \boldsymbol{\nabla}\cdot\boldsymbol{v} = 0 \qquad (2.1a\text{--}c)$$

where $\mathrm{D}/\mathrm{D}t$ is the material derivative, $\boldsymbol{v} = (u, v, w)$ is the velocity vector, ρ_0 and ρ are the ambient reference density and the Boussinesq density difference from ρ_0. Further, p is the pressure field, $\hat{\boldsymbol{k}}$ is the unit vertical vector (positive upward), whilst $\mathcal{D}_m$ represents an m-order viscosity/diffusion operator acting on the momentum and the mass transport, defined as follows (Winters & D'Asaro 1997):

$$\mathcal{D}_m(\cdot) \equiv \begin{cases} \nu_{m,j}\partial_j^{2m} & \text{dissipation,} \\ \kappa_{m,j}\partial_j^{2m} & \text{diffusion,} \end{cases} \quad \text{with } \nu_{m,j} = \kappa_{m,j} \equiv \frac{1}{T_{\mathcal{D}}}\left(\frac{L_j}{\pi n_j}\right)^{2m}, \quad j \in \{x, y, z\}, \quad (2.2)$$

where $\nu_{m,j}$ and $\kappa_{m,j}$ are the m-order viscosity/diffusivity coefficient, respectively, whose physical dimensions are $[L^{2m}/T]$. The operator ∂_j^{2m} corresponds to the $2m$-order partial derivative with respect to the spatial coordinate j (with $j = x, y, z$). L_j and n_j are the

computational domain size and the number of equally spaced grid points in the *j*th direction. $T_{\mathcal{D}}$ is a time scale chosen by trial and error to minimize the range of damped scales while maintaining numerical stability (Winters & D'Asaro 1997). The choice $m = 1$ results in the standard Navier–Stokes equations, which should be solved down to the Kolmogorov length scale which is barely possible given the available computing power. Alternatively, for example, the viscosity could be chosen by trial and error to be just large enough to damp the downscale energy transfer for a given problem resolved over a fixed number of grid points. However, if the goal is to allow the inertial subrange to be as broad as possible for a given grid resolution, then larger values of viscosity are inefficient and smaller values require finer grids to resolve the dissipative scales and maintain stability. Similar arguments apply for the *m*-order operators. We use $m = 3$ for this study and note that the use of this type of closure implicitly assumes a downscale energy cascade with the rate of energy transfer controlled by the nearly inviscid processes in the inertial subrange. This rate can then be measured at small scales by directly evaluating the kinetic energy dissipation rate whose mathematical form depends on the value of *m* chosen as shown in appendix A.

We impose no-flux and free-slip boundary conditions on the top, bottom and sidewalls of the cylindrical domain to avoid having to resolve small viscous boundary layers. The initial condition of the IKW is constructed from the linear normal mode solution derived by Csanady (1967) for a discontinuous two-layer stratification in a cylindrical domain. This solution is written as

$$\eta_i(t, r, \theta)/\eta_0 = \mathrm{I}_1(\beta_1 r) \, \cos(\theta - \omega_1 t - \phi), \qquad (2.3)$$

where $\eta_i(t, r, \theta)$ is the modal structure of the interface displacement and $\beta_1 = R_i^{-1} \sqrt{1 - \sigma_1^2}$. The radial shape of the solution is characterized by the first-kind modified Bessel function of the azimuthal gravest mode, I_1 (Abramowitz & Stegun 1965), while the temporal and azimuthal components are given by the cosine periodic function. The wave frequency, ω_1, and dimensionless frequency, $\sigma_1 = \omega_1/f$, of the IKW are obtained by solving the dispersion relation derived from the boundary condition for η_i at $r = R$ (Csanady 1967; Stocker & Imberger 2003):

$$1 - \sigma_1^2 \mathrm{M}^2 = 0, \quad \text{with } \mathrm{M}^2 \equiv \beta_1 R \frac{\mathrm{I}_0(\beta_1 R)}{\mathrm{I}_1(\beta_1 R)} - 1. \qquad (2.4)$$

From the linearized inviscid governing equations and solution (2.3), we obtain the density and velocity field for a discontinuous two-layer stratification (Csanady 1981; Antenucci & Imberger 2001). However, solution (2.3) cannot be directly used to specify the initial condition of an IKW in a smooth two-layer stratified fluid. Moreover, a derivation of continuous eigenfunctions after introducing a small transition scale δ_i into the density profile is also inconvenient because such solutions are both formally and practically restricted to have displacement amplitudes much smaller than δ_i. Here we wish to study the nonlinear transition regime, and waves in this regime have initial amplitudes substantially larger than δ_i.

For a given $\delta_i \ll h_j$, $j = 1, 2$, the linear, discontinuous solution (2.3) can be specified with an amplitude η_0 significantly larger than δ_i. We prescribe such a solution, expecting that its subsequent evolution will be nonlinear. We then smooth out the discontinuities by allowing the density and momentum to diffuse over a finite time scale such that the interface thickness is of $O(\delta_i)$. In contrast, solving the linear

equations for a continuously varying but sharply transitioning stratification produces overturns in the density field when η_0 approaches or exceeds δ_i (see e.g. Kundu & Cohen (2004), Chapter 13, on normal modes in a continuously stratified layer).

The equations of motion (2.1), with the smoothed version of the initial condition (2.3), are numerically solved using the three-dimensional spectral model flow_solve (Winters & de la Fuente 2012). The model is based on expansions in terms of trigonometric functions of the dependent variables over regular meshes in a cubic domain (L_x, L_y, L_z), inside which a cylindrical domain (R, H) is immersed. The variables are expanded in cosine or sine series in each spatial component, depending on the boundary conditions to be satisfied. For example, in the vertical direction, the horizontal velocity components, u and v, and the density field, ρ, are expanded in cosine series while the vertical velocity component, w, is expanded in sine series to satisfy the free-slip wall and no-flux condition on the top and bottom boundaries. The boundary conditions on the curved sidewall are implemented using an immersed boundary approach introduced by Winters & de la Fuente (2012).

2.2. *Dimensionless numbers*

The initial dynamics of the IKW are parametrized by four dimensionless parameters:

$$\mathcal{B}_i \equiv \frac{R_i}{R}, \quad \mathcal{T}_{sk} \equiv \frac{\lambda_k}{\Delta c_i T_k}, \quad \mathcal{T}_{vk} \equiv \frac{\eta_0^{2m}}{\nu_m T_k}, \quad \mathcal{J} \equiv \frac{\mathcal{N}^2}{\mathcal{S}^2}. \qquad (2.5a\text{--}d)$$

Here $\mathcal{B}_i$ is the Burger number (Antenucci & Imberger 2001) that characterizes the influence of rotation. If $\mathcal{B}_i \geqslant 1$, rotation is weak, while if $\mathcal{B}_i < 1$, rotational effects are important. In the IKW case, as $\mathcal{B}_i \to 0$, the wave energy becomes concentrated near the boundary with the fluid motions parallel to the shoreline. Notice that $\mathcal{B}_i$ corresponds to the positive root of the classic Burger number, S, defined by Pedlosky (1987, see § 1.3, equation 1.3.1).

$\mathcal{T}_{sk}$ is the steepening parameter and it is interpreted as the rate at which the spatial differences of the internal wave celerity induced by η_0 lead to wavefronts and nonlinearities, $T_s \sim \lambda_k/\Delta c_i$, over an IKW period T_k. Therefore, $\mathcal{T}_{sk}$ quantifies how fast an IKW with amplitude η_0 tends to produce a nonlinear wavefront (Boegman, Ivey & Imberger 2005; de la Fuente *et al.* 2008) and thus to concentrate energy at smaller length scales in the near-shore region.

$T_{vk} \sim \eta_0^{2m}/\nu_m$ is the dissipation time scale for motions of vertical scale η_o and $\mathcal{T}_{vk}$ gives the ratio of this time scale to the Kelvin wave period. To quantify the relative importance of viscous to nonlinear effects in the context of this flow, we have defined a dimensionless number that is the ratio of the (hyper-)viscous time scale to the nonlinear steepening time of the primary Kelvin wave:

$$\frac{\mathcal{T}_{vk}}{\mathcal{T}_{sk}} \equiv \frac{\Delta c_i \eta_0^{2m-1}}{\nu_m} \left(\frac{\eta_0}{\lambda_k} \right). \qquad (2.6)$$

In this sense, this ratio is similar to the standard Reynolds number that relates inertial to viscous forces. The definition of the m-order hyper-viscous Reynolds number is (Lamorgese, Caughey & Pope 2005; Spyksma *et al.* 2012)

$$Re_m \equiv \frac{\Delta c_i \eta_0^{2m-1}}{\nu_m}, \qquad (2.7)$$

which formally reduces to the classic viscous Reynolds number when $m = 1$:

$$Re \equiv \frac{\Delta c_i \eta_0}{\nu_m}. \tag{2.8}$$

High values of Re_m imply energetic regimes, dominated by inertial forces, whereas low values of Re_m imply flow regimes dominated by (hyper-)viscous forces. The parameter $\mathcal{T}_{vk}/\mathcal{T}_{sk}$ can be written in terms of the hyper-viscous Reynolds number as follows:

$$\frac{\mathcal{T}_{vk}}{\mathcal{T}_{sk}} \equiv Re_m \left(\frac{\eta_0}{\lambda_k} \right). \tag{2.9}$$

Note that η_0/λ_k is the aspect ratio of the Kelvin wave and it is a measure of its hydrostaticity. Steeper, non-hydrostatic waves are more nonlinear and enhance the energy transfer to small scales.

$\mathcal{J}$ is the gradient Richardson number, with $\mathcal{N}$ the buoyancy frequency and $\mathcal{S}$ the vertical shear in the horizontal velocity (Miles 1961). In our problem, both $\mathcal{N}$ and $\mathcal{S}$ have maxima at the height of the density interface but the magnitude and spatial distribution of $\mathcal{J}$ will depend both on η_0 and $\mathcal{B}_i$. The maximal shear $\mathcal{S}$, for example, occurs in the shore region, near the maximum vertical displacement of the interface. For a fixed rotation regime, the initial minimum value of $\mathcal{J}$ decreases as η_0 is increased.

The dissipation and mixing involved in the IKW evolution are characterized in terms of dimensionless turbulence activity parameters that quantify the dissipation rates of kinetic energy and buoyancy variance given by

$$\mathcal{I}_m \equiv \frac{1}{\mathcal{N}^2} \left\{ \frac{(\epsilon_m)^m}{\nu_m} \right\}^{2/(3m-1)}, \qquad \mathcal{K}_m \equiv |\nabla^m b|^2 \left| \frac{\mathrm{d}^m b}{\mathrm{d} z_*^m} \right|^{-2} \tag{2.10a,b}$$

where $\mathcal{I}_m$ denotes the turbulence intensity parameter expressed in terms of the hyper-viscosity approach of the kinetic energy dissipation rate, ϵ_m, and derived from the ratio of the Ozmidov and Kolmogorov scales (see appendix A). This parameter can be interpreted as the destabilizing effects of turbulent stirring compared to the stabilizing effects produced by the combined action of hyper-viscosity and buoyancy. Finally, $\mathcal{K}_m$ is the ratio of the diapycnal flux and a reference laminar diffusive flux, both in terms of the hyper-diffusion approach and the buoyancy, b. This diffusivity parameter measures the increase in diffusive flux due to turbulent stirring and straining relative to the laminar, diffusive flux with the same background buoyancy that is not stirred or strained (see appendix B).

2.3. *Set of numerical experiments*

We consider a single rotation regime, $\mathcal{B}_i = 0.25$, and a range of dimensionless amplitudes $\eta_0/h_1 \in [0.07, 0.60]$ and aspect ratios $\eta_0/\lambda_k \in [8.8 \times 10^{-4}, 7.5 \times 10^{-3}]$ that allow $\mathcal{T}_{sk} \in [3.6, 34.6]$, $\mathcal{T}_{vk} \in [10^{-1}, 4 \times 10^4]$ and initial minimum values of $\mathcal{J}$ between $\min\{\mathcal{J}_0\} = 31.86$, for $\eta_0/h_1 = 0.07$, and $\min\{\mathcal{J}_0\} = 0.13$, for $\eta_0/h_1 = 0.60$. With these parameters, we have performed six numerical experiments using spatial and temporal scales similar to those used in recent laboratory experiments carried out in a rotating table by Ulloa *et al.* (2014). The dimensions of the domain are $L_x \times L_y \times L_z = 1.95 \times 1.95 \times 0.2$ m³, and in its interior there is a circumscribed cylinder of radius $R = 0.9$ m and depth $H = h_1 + h_2 = 0.07$ m $+ 0.13$ m $= 0.2$ m.
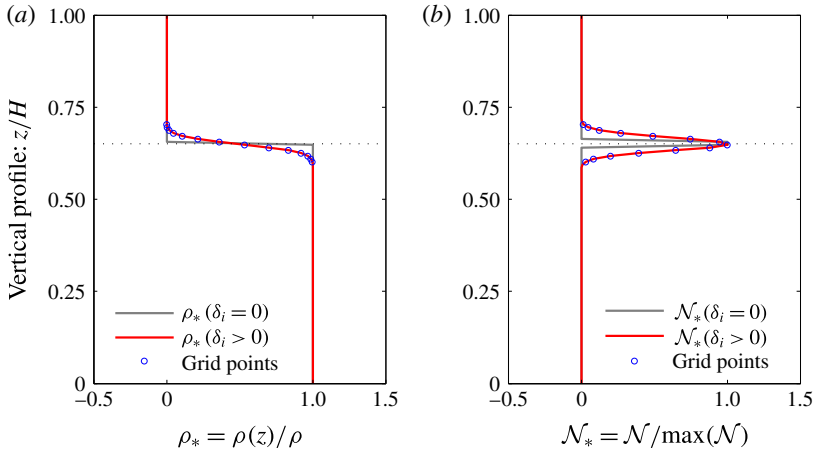
FIGURE 2. Density, $\rho(z)/\rho$, and buoyancy frequency, $\mathcal{N}(z)/\max(\mathcal{N})$, profiles in the initial condition of a discontinuous two-layer stratification $\delta_i = 0$ (grey line) and a smooth two-layer stratification $\delta_i > 0$ (red line) after a vertical diffusion over a time interval t_{δ_i}. The blue circles denote the equidistant grid points along the transition layer.

The difference of densities is $\Delta\rho = \rho_2 - \rho_1 = 15$ kg m^{-3}, the effective thickness of the interfacial transition is $\delta_i \approx 0.02$ m, and the inertial frequency $f = 0.361$ Hz, with an IKW period of $T_k = 60.45$ s and a total simulation time $T_{ns} = 3T_k = 182$ s. Figure 2 shows that the initial transition layer is resolved by about 12–14 grid points. The horizontal wavelength of the most unstable mode for a smooth, sheared density transition is about π times the interface thickness (see e.g. Kundu & Cohen 2004, § 11.7, p. 506). This corresponds to about 10–11 times our horizontal grid spacing and so the most unstable mode is resolved on our spatial grid, though significantly smaller motions are not. Table 2 summarizes the parameters used in the numerical experiments.

3. Dynamic regimes

Figure 3 illustrates the time series of a density profile at $r/R = 0.98$ and $\theta = 0$ where $\eta_i(t = 0, 0.98 R, 0) \approx \eta_0$, and the power spectral density (PSD) of the density interface displacement $\eta_i(t, 0.98 xR, 0)$. The IKW response is classified into four distinct regimes: the damped linear (DLR), nonlinear (NLR), nonlinear/non-hydrostatic (NHR) and laminar–turbulent transition regime (TR). The regimes have been defined in terms of their dynamical characteristics ($\mathcal{T}_{sk}$, $\mathcal{T}_{vk}$, $\mathcal{J}$) and via visual inspection of the density field evolution, similar to the terms in which Horn, Imberger & Ivey (2001) classified the degeneration of large-scale internal waves in a non-rotating basin. We examine each regime in the following subsections.

3.1. *Damped linear regime (DLR)*

The DLR is characterized by the evolution of an IKW that retains most of its initial linear features, with negligible nonlinear steepening and strongly controlled by viscosity. This regime describes the results of experiment 1 shown in figure 3(*a,b*); in this case, $\eta_0/h_1 = 0.07$ ($\eta_0/\delta_i \approx 1.0$), $\mathcal{T}_{vk}/\mathcal{T}_{sk} \approx 3 \times 10^{-3} < 1$ and $\min\{\mathcal{J}_0\} \approx 31.86$, which suggests an extremely viscous flow with a negligible steepening capacity and a strong hydrodynamic stability in the density interface. Therefore a linear and damped

Symbol	Dimensions	Property	Definition	Location
$\eta_i(t, \boldsymbol{x})$, $\eta_i(t, r, \theta)$	m	Vertical displacement of density interface in Cartesian and polar coordinates		§1, figure 1, (2.3)
η_0	m	Initial wave amplitude	$\max\{\eta_i(t=0, \boldsymbol{x})\}$	§1, figure 1
h_ℓ, $\ell = 1, 2$	m	Thickness of the ℓth layer	$h_1 = 0.07$, $h_2 = 0.13$	§1, figure 1
H	m	Depth of the cylindrical basin	$h_1 + h_2 = 0.2$	§1, figure 1
η_0/h_1	—	Dimensionless amplitude	$\in [0.07, 0.60]$	§1, figure 1
δ_i	m	Length scale of the transition layer	≈ 0.02	§2.1, figure 1
λ_k	m	Wavelength of the IKW	$2\pi R$	§2.2, (2.5)
ρ_ℓ, $\ell = 1, 2$	kg m^{-3}	Density of the ℓth layer	$\rho_1 = 1000$, $\rho_1 = 1015$	§1, figure 1
$\Delta \rho$	kg m^{-3}	Density difference	$\rho_2 - \rho_1 = 15$	§1
g	m s^{-2}	Gravity acceleration	9.81	§1, figure 1
g'	m s^{-2}	Reduced gravity acceleration	$(\Delta\rho/\rho_0)g \approx 0.147$	§1
c_i	m s^{-1}	Linear internal celerity	$\sqrt{g' h_1 h_2 / H} \approx 0.082$	§1
f	s^{-1}	Inertial frequency	0.361	§1, figure 1
R	m	Radius of the cylindrical basin	0.9	§1, figure 1
D	m	Diameter of the cylindrical basin	$2R = 1.8$	§1, figure 1
R_i	m	Internal Rossby radius of deformation	$c_i/f \approx 0.225$	§1, figure 1
$\boldsymbol{v}$	m s^{-1}	Velocity field	(u, v, w)	§2.1, (2.1)
ρ_0	kg m^{-3}	Ambient reference density	1000	§2.1, (2.1)
ρ	kg m^{-3}	Boussinesq density difference from ρ_0		§2.1, (2.1)
p	Pa	Pressure field		§2, (2.1)
L_j, $j = x, y, z$	m	Computational domain size in the jth coordinate	$L_x \times L_y \times L_z = 1.95 \times 1.95 \times 0.2$	§2.1, (2.2)
n_j, $j = x, y, z$	—	Number of grid points in the jth coordinate		§2.1, (2.2), table 2
k_v	m^{-1}	Vertical grid wavenumber		§2.3

TABLE 1. Continued on next page.

k_r, k_θ	m^{-1}	Horizontal grid wavenumber in cylindrical coordinates		§2.3
k_{δ_i}	m^{-1}	Wavenumber associated with the interfacial transition scale		§2.3
k_h^{KH}	m^{-1}	Wavenumber of the most unstable interfacial wave	$\approx 2\pi/(7\delta_i)$	§2.3
$\nu_{m,j}$	m^{2m} s^{-1}	Hyper-viscosity coefficient	$T_\mathcal{D}^{-1}\left(\dfrac{L_j}{\pi n_j}\right)^{2m}$	§2.1, (2.2)
$\kappa_{m,j}$	m^{2m} s^{-1}	Hyper-diffusivity coefficient	$T_\mathcal{D}^{-1}\left(\dfrac{L_j}{\pi n_j}\right)^{2m}$	§2.1, (2.2)
$T_\mathcal{D}$	s	Numerical damping time scale		§2.1, (2.2)
$\mathcal{D}_m(\cdot)$	s^{-1}	m-order viscosity/diffusion operator	$\begin{cases}\nu_{m,j}\partial_j^{2m} & \text{dissipation}\\ \kappa_{m,j}\partial_j^{2m} & \text{diffusion}\end{cases}$	§2.1, (2.2)
I_1	—	First-kind modified Bessel function of order 1		§2.1, (2.3)
ϕ	rad	Phase of wave	0	§2.1, (2.3)
ω_1	s^{-1}	Wave frequency of the Kelvin gravest mode	≈ 0.104	§2.1, (2.3)
σ_1	—	Dimensionless wave frequency of the Kelvin gravest mode	$\omega_1/f \approx 0.288$	§2.1, (2.4)
$\mathcal{B}_i$	—	Burger number	$R_i/R \approx 0.25$	§2.2, (2.5)
T_k	s	Kelvin wave period	≈ 60.45	§2.2, (2.5)
$\mathcal{T}_{sk}$	—	Steepening parameter	$\lambda_k/(\Delta c_i T_k) \in [3.6,\ 34.6]$	§2.2, (2.5), table 2
$\mathcal{T}_{vk}$	—	Damping parameter	$\eta_0^{2m}/(\nu_m T_k) \in [10^{-1},\ 4\times10^4]$	§2.2, table 2
$\mathcal{T}_{vk}/\mathcal{T}_{sk}$	—	Ratio of advective to viscous forces	$\Delta c_i\eta_0^{2m}/(\nu_m\lambda_k) \in [3\times10^{-3},\ 10^4]$	§2.2, table 3
Re_m	—	Hyper-viscous Reynolds number	$\Delta c_i\eta_0^{2m-1}/\nu_m$	§2.2, (2.7)
Re	—	Reynolds number ($m=1$)	$\Delta c_i\eta_0/\nu$	§2.2, (2.8)
$\mathcal{N}$	s^{-1}	Buoyancy frequency	$\sqrt{g\rho_0^{-1}\partial_z\rho}$	§2.2, (2.5)
$\mathcal{N}_0$	s^{-1}	Maximum buoyancy frequency	$\max\{\mathcal{N}(t=0,\boldsymbol{x})\}$	§4.3
$T_{\mathcal{N}_0}$	s	Buoyancy period at the pycnocline	$2\pi/\mathcal{N}_0 \approx 1$	§2.3

TABLE 1 (cntd). Continued on next page.

Symbol	Units	Description	Definition	Reference
$\mathcal{S}$	s^{-1}	Vertical shear in the horizontal velocity	$\sqrt{(\partial_z U)^2 + (\partial_z V)^2}$	§4.3
$\mathcal{J}$	—	Gradient Richardson number	$\mathcal{N}^2/\mathcal{S}^2$	§2.2, (2.5)
$\mathcal{J}_0$	—	Gradient Richardson number at $t=0$	$\mathcal{J}(t=0,\boldsymbol{x})$	§2.3, table 2
T_{ns}	s	Total simulation time	$3T_k \approx 181.35$	§2.3
ϵ_m	m^2 s^{-3}	Hyper-viscous kinetic energy dissipation rate	$\nu_m|\nabla^m\boldsymbol{v}|^2$	§2.2, (2.10), appendix A, (A4)
$\mathcal{I}_m$	—	Turbulence intensity parameter	$\mathcal{N}^{-1}\{(\epsilon_m)^m/\nu_m\}^{2/(3m-1)}$	§2.2, (2.10), appendix A, (A9)
$\langle\mathcal{I}_m\rangle_H$	—	Vertical average of $\mathcal{I}_m$	$H^{-1}\int_0^H \mathcal{I}_m\,\mathrm{d}\tilde{z}$	§4
$\langle\mathcal{I}_m\rangle_V$	—	Bulk average of $\mathcal{I}_m$	$V^{-1}\int_V \mathcal{I}_m\,\mathrm{d}\tilde{V}$	§4.2, table 3
$\langle\mathcal{I}_m\rangle_{V,T}$	—	Spatial and temporal average of $\mathcal{I}_m$	$(T_{ns})^{-1}\int_{T_{ns}}\left\{V^{-1}\int_V \mathcal{I}_m\,\mathrm{d}\tilde{V}\right\}\mathrm{d}\tilde{t}$	§4.2
b	m s^{-2}	Buoyancy field	$(1-\rho/\rho_0)g$	§2.2, (2.10), appendix B, (B6)
z_*	m	Reference height in the minimum potential energy state of a fluid		§2.2, (2.10), appendix B, (B1)
$\mathcal{K}_m$	—	Diffusivity parameter	$|\nabla^m b|^2\,|\mathrm{d}^m b/\mathrm{d}z_*^m|^{-2}$	§2.2, (2.10), appendix B, (A8)
$\langle\mathcal{K}_m\rangle_V$	—	Bulk average of $\mathcal{K}_m$	$V^{-1}\int_V \mathcal{K}_m\,\mathrm{d}\tilde{V}$	§4.2, table 3
$\langle\mathcal{K}_m\rangle_{V,T}$	—	Spatial and temporal average of $\mathcal{K}_m$	$(T_{ns})^{-1}\int_{T_{ns}}\left\{V^{-1}\int_V \mathcal{K}_m\,\mathrm{d}\tilde{V}\right\}\mathrm{d}\tilde{t}$	§4.2
z_i	m	Height of the density interface ($\rho(t,\boldsymbol{x})=\Delta\rho/2$)		§4
$\mathcal{A}_\theta$	—	Area defined by $z/H\in[0,1]$, $\theta\in[0,2\pi]$ and $r/R=0.98$		§4.3
$\boldsymbol{\omega}$	s^{-1}	Vorticity field	$\nabla\times\boldsymbol{v}$	§4.3.1
ℓ_K	m	Hyper-viscous Kolmogorov length scale	$\{\nu_m^3/\epsilon_m\}^{1/(6m-2)}$	Appendix A, (A5)
ℓ_O	m	Ozmidov length scale	$\{\epsilon_m/\mathcal{N}^3\}^{1/2}$	Appendix A, (A6)

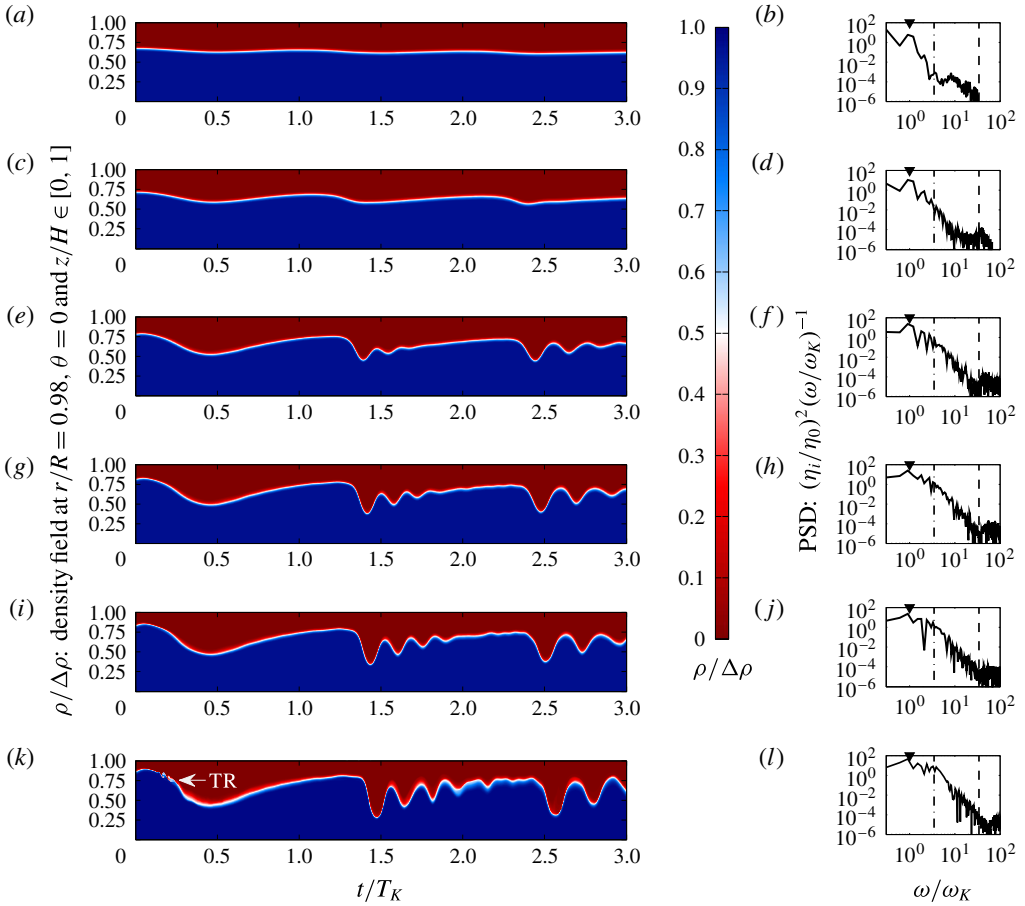TABLE 1 (cntd). Glossary of symbols used in the text.

FIGURE 3. (a,c,e,g,i,k) Time series of density field along the vertical profile where the maximum wave amplitude is achieved. (b,d,f,h,k,l) PSD of vertical displacement of density interface η_i: ▼, Kelvin wave frequency; –·–·–, inertial frequency (f/ω_k); – – –, initial buoyancy frequency ($\mathcal{N}_0/\omega_K$); TR, transition regime. (a,b) Exp. 1, $\eta_0/h_1 = 0.07$; (c,d) exp. 2, $\eta_0/h_1 = 0.18$; (e,f) exp. 3, $\eta_0/h_1 = 0.38$; (g,h) exp. 4, $\eta_0/h_1 = 0.47$; (i,j) exp. 5, $\eta_0/h_1 = 0.54$; (k,l) exp. 6, $\eta_0/h_1 = 0.60$.

Exp.	η_0/δ_i	η_0/h_1	η_0/λ_k	$\mathcal{B}_i$	$\mathcal{T}_{sk}$	$\mathcal{T}_{vk}$	$\mathcal{T}_{vk}/\mathcal{T}_{sk}$	$\min_{z \sim z_i}\{\mathcal{J}_0\}$	n_x	n_y	n_z
1	1.0	0.07	8.8×10^{-4}	0.25	3.5×10^1	10^{-1}	3×10^{-3}	31.86	321	321	129
2	2.5	0.18	2.2×10^{-3}	0.25	1.4×10^1	2.7×10^1	2×10^0	3.04	321	321	129
3	5.3	0.38	4.7×10^{-3}	0.25	6.2×10^0	2.5×10^3	4×10^2	0.58	321	321	129
4	6.6	0.47	5.8×10^{-3}	0.25	4.9×10^0	8.8×10^3	2×10^3	0.30	321	321	129
5	7.5	0.54	6.7×10^{-3}	0.25	4.2×10^0	2.0×10^4	5×10^3	0.19	321	321	129
6	8.4	0.60	7.5×10^{-3}	0.25	3.6×10^0	4.0×10^4	10^4	0.13	513	513	129

TABLE 2. Summary of the dimensionless parameters of the experimental sets.

IKW dynamics along the $3T_k$ periods is expected. The PSD in figure 3(b) shows a single strong energy peak at $\omega/\omega_k = 1$, indicating that the initial IKW mode stored the energy of the flow.

3.2. *Nonlinear regime (NLR)*

The NLR is characterized by weak nonlinear degeneration, without dispersion of the IKW (in the KdV theory sense). This regime starts with the IKW steepening, as a consequence of a wave amplitude large enough to induce significant changes in the wave celerity, leading the wavefront and the formation of a solitary-type wave (Fedorov & Melville 1995; de la Fuente *et al.* 2008). This regime describes the results of experiment 2 shown in figure 3(*c,d*); in this case $\eta_0/h_1 = 0.18$, $\mathcal{T}_{vk}/\mathcal{T}_{sk} \approx 1.9 > 1$ and min$\{\mathcal{J}_0\} \approx 3.04$, and therefore we expect a weakly nonlinear steepening controlled by viscosity and a stable flow around the density interface. In fact, figure 3(*c*) shows a slightly steep wavefront after the first wave period and a solitary-type wave structure around $t/T_k \approx 2.45$. The PSD in figure 3(*d*) shows a wider energy cascade due to transfer of energy involved in the weakly nonlinear degeneration, with a main energy peak at $\omega/\omega_k = 1$, and two lower peaks of sub-inertial frequencies attributed to sub-azimuthal Kelvin waves (see the dot-dashed line).

3.3. *Nonlinear and non-hydrostatic regime (NHR)*

Nonlinear steepening and non-hydrostatic dispersion of the initial IKW (in the KdV theory sense) characterize the NHR. As the wave steepens, its azimuthal length scale decreases until the non-hydrostatic terms can be important enough to balance the nonlinear steepening, avoiding the wave breaking (Helfrich & Melville 2006) and leading the degeneration of the IKW into a package of solitary-type waves (Grimshaw 1985). This process induces an important energy cascade from the basin scale to smaller scales. The NHR regime is identified in experiments 3–6 (see figures 3*e–l*). In these experiments the Reynolds number increases from $\mathcal{T}_v/\mathcal{T}_s \approx 4 \times 10^2$, for $\eta_0/h_1 = 0.38$, to $\mathcal{T}_{vk}/\mathcal{T}_{sk} \approx 10^4$, for $\eta_0/h_1 = 0.60$. Increasing $\mathcal{T}_v/\mathcal{T}_s$ corresponds to increasing nonlinearity and concentration of energy at smaller scales. Experiments 3 and 4 show hydrodynamic stable flows in the density interface region, with min$\{\mathcal{J}_0\} \approx 0.58$ and min$\{\mathcal{J}_0\} \approx 0.30$, respectively, whereas experiments 5 and 6 show evidence of the emergence of hydrodynamic interfacial instabilities, with min$\{\mathcal{J}_0\} \approx 0.20$ and min$\{\mathcal{J}_0\} \approx 0.13$, respectively.

3.4. *Laminar–turbulent transition regime (TR)*

The TR is characterized by the growth and occurrence of interfacial instabilities. Depending on how energetic the shear flow is, the instabilities can grow and generate turbulent patches in the density interface region or can be damped. The hydrodynamic stability of the IKW sheared flow can be studied via the gradient Richardson number, $\mathcal{J}$, whose critical value $\mathcal{J} = 0.25$ (Miles 1961) is neither a necessary nor a sufficient condition to trigger interfacial instabilities in our sheared-type flow, but it is still a very useful criterion that can give us an order of magnitude. In our results only two experiments show the presence of interfacial instabilities, experiments 5 and 6, with min$\{\mathcal{J}_0\} \approx 0.20$ and min$\{\mathcal{J}_0\} \approx 0.13$, respectively. Only they have initial $\mathcal{J} < 0.25$. Both experiments exhibit the emergence of Kelvin–Helmholtz-type billows on the wavefront of strongly nonlinear IKWs ($\mathcal{T}_{vk}/\mathcal{T}_{sk} \sim 5 \times 10^3$–$10^4$). However, the results of experiment 5 show fast damping of the interfacial instabilities, while the results of experiment 6 show a complex spatial and temporal dynamic, in which large scales, attributed to the IKW and internal solitary-type waves, coexist and interplay with turbulent small scales, associated with interfacial instabilities/breaking and turbulent patches.
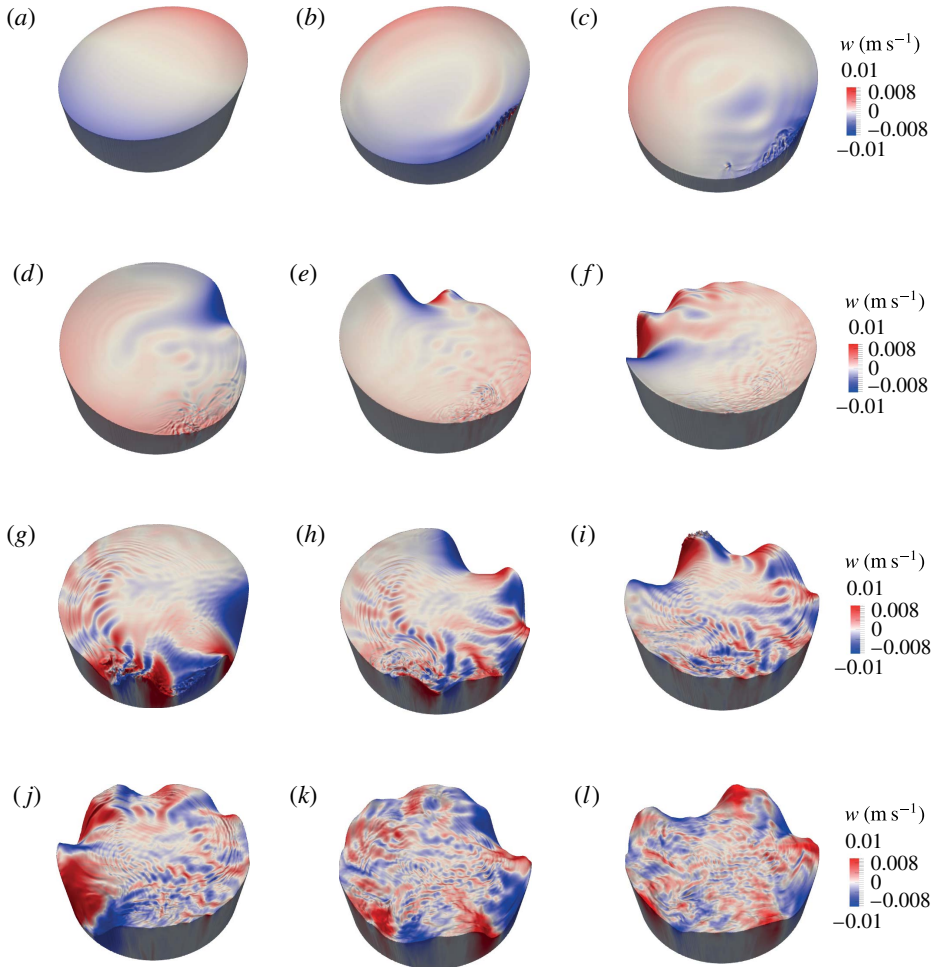
FIGURE 4. Results of experiment 6: evolution in time $t/T_k \in [0, 3]$ of the vertical velocity w at the density interface region $\rho(t, \boldsymbol{x}) = \Delta\rho/2$. (a) $t/T_k = 0$, (b) $t/T_k = 0.128$, (c) $t/T_k = 0.25$, (d) $t/T_k = 0.5$, (e) $t/T_k = 0.75$, (f) $t/T_k = 1.0$, (g) $t/T_k = 1.5$, (h) $t/T_k = 1.75$, (i) $t/T_k = 2.0$, (j) $t/T_k = 2.25$, (k) $t/T_k = 2.75$, (l) $t/T_k = 3.0$.

The first three regimes have been analysed in previous numerical (de la Fuente *et al.* 2008; Sakai & Redekopp 2010) and experimental studies (Wake, Ivey & Imberger 2005; Ulloa *et al.* 2014), whereas the TR on IKWs has been observed only in field data (Lorke 2007; Preusse *et al.* 2010) and to date in numerical experiments.

4. Internal Kelvin wave: transition from laminar to turbulent regime

Hereafter we focus on the spatial and temporal evolution of the IKW in the TR (analysing results of experiment 6), aiming to link the dynamic wave response with turbulent activity. Figure 4 shows the evolution of the vertical velocity, $w(t, r, \theta, z)$, at the density interface z_i to illustrate the strongly nonlinear dynamics of the IKW in experiment 6. Here $z_i(t)$ is defined as the vertical position of the $\rho(t, \boldsymbol{x}) = \Delta\rho/2$ iso-scalar surface. Figure 4(a) shows the initial condition of the IKW

$(t/T_k = 0)$. The degeneration of the IKW begins with the emergence of instabilities of Kelvin–Helmholtz (KH) type on the wavefront that starts to steepen at $t/T_k = 0.128$ (see figure 4b); it is in this region where the minimum Richardson number, $\mathcal{J} \approx 0.13$, is achieved. Figures 4(c) and 4(d) ($t/T_k \in [0.25, 0.5]$) show the formation of a turbulent patch induced by the breakdown of the KH-type billows; this patch evidences a slight spread along the azimuthal and radial axes. Figure 4(d) shows the formation of the first solitary-type wave around $t/T_k \in [0.5, 0.625]$, while figures 4(e) and 4(f) show a solitary wave train confined to the near-shore region around $t/T_k \in [0.75, 1.0]$. After the first IKW period (see figure 4f,g) the leading wave starts to interact with the pre-existing turbulent patch. This interaction is accompanied by the regrowth of interfacial instabilities upstream of the wavefront and a subsequent interfacial turbulent wake on the solitary wave train (see figure 4g). The regrowth of interfacial instabilities generate a new turbulent patch that holds the same azimuthal location while it is vertically advected upward and downward by the solitary wave train (see figure 4h). During and after the interaction between the large internal waves and the turbulent patch, inertial waves of different scales are radiated to the offshore region (see figure 4h–k). At $t/T_k = 3$ (see figure 4l) there is no longer evidence of the initial IKW; the internal waves in the near-shore region have decayed in amplitude, whilst a range of smaller length scales have been excited in the interior. During the first three IKW periods we observe that different nonlinear processes coexist, enhancing the degeneration of the initial long wave and promoting a forward energy cascade.

4.1. *Spatiotemporal distribution of turbulence*

Figure 5 shows the vertical average of the turbulence intensity parameter, $\langle \mathcal{I}_m \rangle_H$; the dashed line defines the radial position of the internal Rossby radius of deformation, R_i, from the boundary to the interior. Figure 5(a) shows the initial distribution of $\langle \mathcal{I}_m \rangle_H$ induced by the IKW itself. Kinetic energy dissipation is concentrated within R_i and decays to low values towards the centre of the domain. The nonlinear dynamics of the IKW induces distinct zones of elevated values in the near-shore region, associated with turbulent patches produced by the breakdown of interfacial instabilities (see figure 5b–d). As the initial IKW degenerates, the turbulence intensity increases at the front of each solitary-type wave along the shore region (see figure 5d–f) achieving values of $\langle \mathcal{I}_m \rangle_H \sim O(10^2)$, while most of the offshore region shows a low activity with values of $\langle \mathcal{I}_m \rangle_H \sim O(10^{-1})$. However, after the first period, and particularly after the strong reactivation of the pre-existing turbulent patch, there is a steady increase of $\langle \mathcal{I}_m \rangle_H$ to the interior of R_i, with values in the range $O(10^0) \leqslant \langle \mathcal{I}_m \rangle_H \leqslant O(10^1)$ (see figure 5f–h). This process is again observed after the second period (see figure 5j). After three periods elevated values of $\langle \mathcal{I}_m \rangle_H$ are distributed throughout the domain (see figure 5k,l). Nevertheless, there are clear differences in the intensity between the near-shore and interior regions, where the internal Rossby radius of deformation (dashed line) seems to define a transition length scale of the turbulent activity along the radial component.

The azimuthal distribution of the turbulence intensity parameter has features of baroclinic instabilities. This is also observed in figure 6, which shows the relative vertical vorticity, $\boldsymbol{\omega} \cdot \hat{\boldsymbol{k}}$, normalized by f at $z/H = 0.8$ (horizontal plane) and the density interface structure $\rho(t, \boldsymbol{x}) = \Delta \rho / 2$ in purple. Initially we observe the formation of one turbulent patch in the shore region around $t/T_k = 0.25$ (see figure 6c), which grows and spreads along the shore until approximately the first period (see figure 6d–f). After the first period, the initial turbulent patch is separated into two (see figure 6d,h,i)
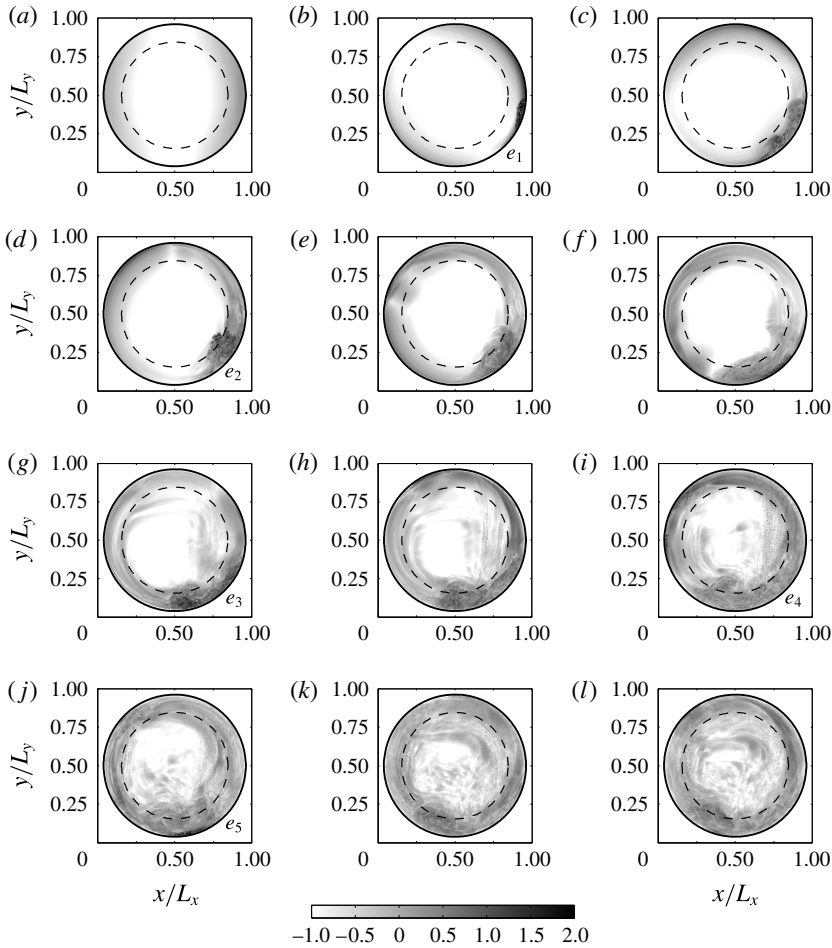
FIGURE 5. Results of experiment 6: spatiotemporal distribution of the turbulence intensity, $\langle \mathcal{I}_m \rangle_H$. (*a*) $t/T_k = 0$, (*b*) $t/T_k = 0.128$, (*c*) $t/T_k = 0.25$, (*d*) $t/T_k = 0.5$, (*e*) $t/T_k = 0.75$, (*f*) $t/T_k = 1.0$, (*g*) $t/T_k = 1.5$, (*h*) $t/T_k = 1.75$, (*i*) $t/T_k = 2.0$, (*j*) $t/T_k = 2.25$, (*k*) $t/T_k = 2.75$, (*l*) $t/T_k = 3.0$.

that also remain trapped on the shore, and a third vortex structure grows on the shore region during the second period (see figure 6*k*,*l*). It is observed that turbulent patches tend to aggregate in large horizontal motions that scale with R_i. Figure 6(*m*) shows a close-up of the vertical vorticity at $t/T_k = 3$, where three large-scale vortex-type motions are identified in the near-shore region (see dashed ellipses). We can study the existence of baroclinic instability via a simplified model. Pedlosky (1970) considered a quasi-geostrophic two-layer model in an inviscid flow rotating on an f-plane, with uniform velocities U_1 and U_2 in each layer ($U_1 \neq U_2$). The flow is unstable to disturbances with horizontal wavelengths, λ, larger than πR_i (see e.g. Pedlosky 1987, Chapter 7, p. 556). Then, considering the azimuthal wavelength of the IKW, $\lambda_k = 2\pi R$, and the internal Rossby radius here adopted, it is obtained that the flow induced by the IKW admits the growth of baroclinic instabilities because $\pi R_i / \lambda_k = \mathcal{B}_i / 2 = 0.125$. In addition, the interaction between the vortex-type motions and the vertical shear flow driven by the IGW could be supporting the emergence of baroclinic instabilities
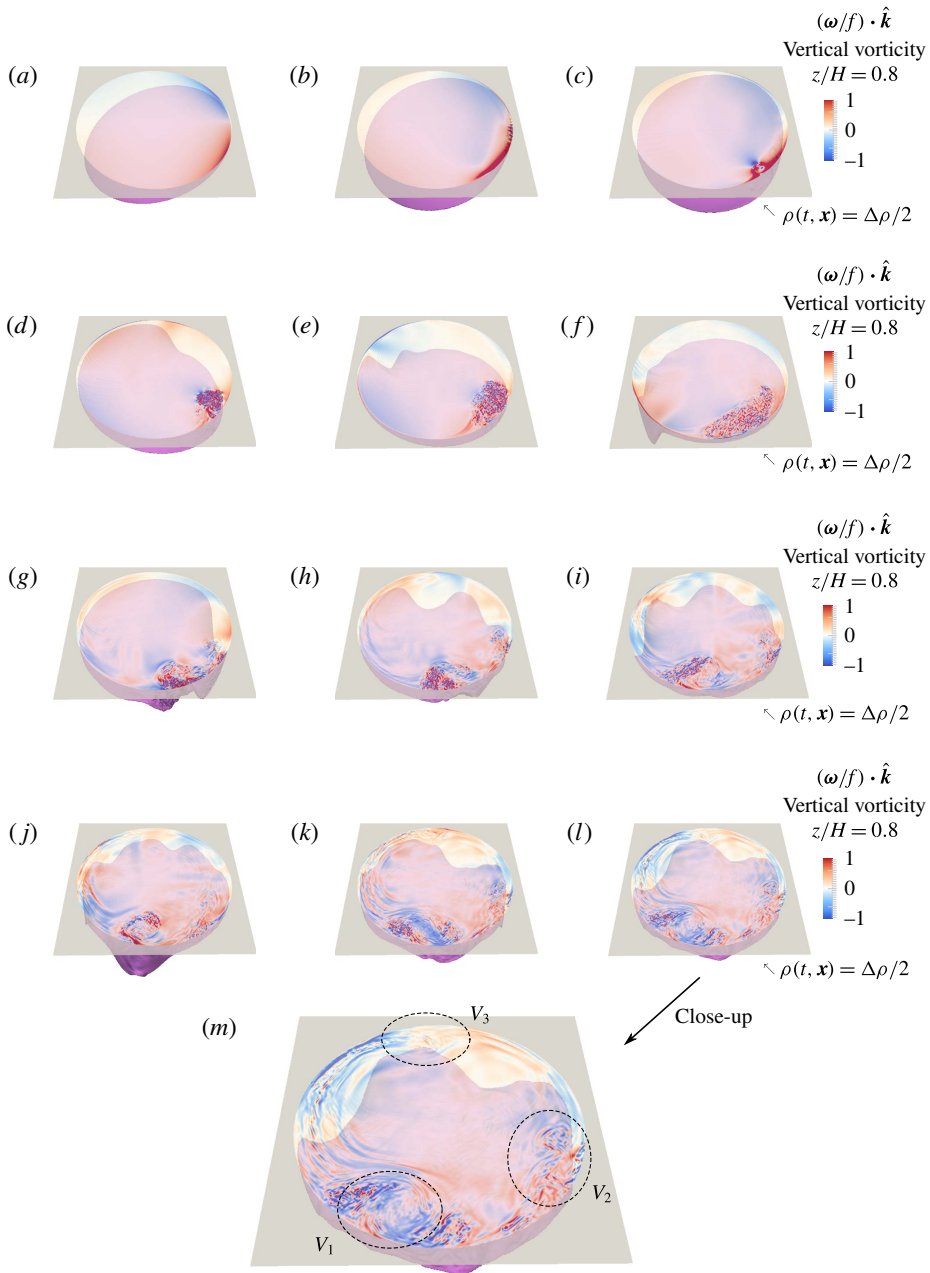
FIGURE 6. Results of experiment 6: spatiotemporal distribution of the vertical vorticity, $(\boldsymbol{\omega}/f) \cdot \hat{\boldsymbol{k}}$, at $z/H = 0.80$. (a) $t/T_k = 0$, (b) $t/T_k = 0.128$, (c) $t/T_k = 0.25$, (d) $t/T_k = 0.5$, (e) $t/T_k = 0.75$, (f) $t/T_k = 1.0$, (g) $t/T_k = 1.5$, (h) $t/T_k = 1.75$, (i) $t/T_k = 2.0$, (j) $t/T_k = 2.25$, (k) $t/T_k = 2.75$, (l) $t/T_k = 3.0$, (m) $t/T_k = 3.0$.

(Sakai 1989; Gula, Plougonven & Zeitlin 2009; Flór, Scolan & Gula 2011). Note that these large-scale vortex motions are not observed in the interior of the basin.

Figure 7 shows the time series of extreme and bulk values of the turbulence intensity parameter, within and outside R_i. The red vertical lines identify events
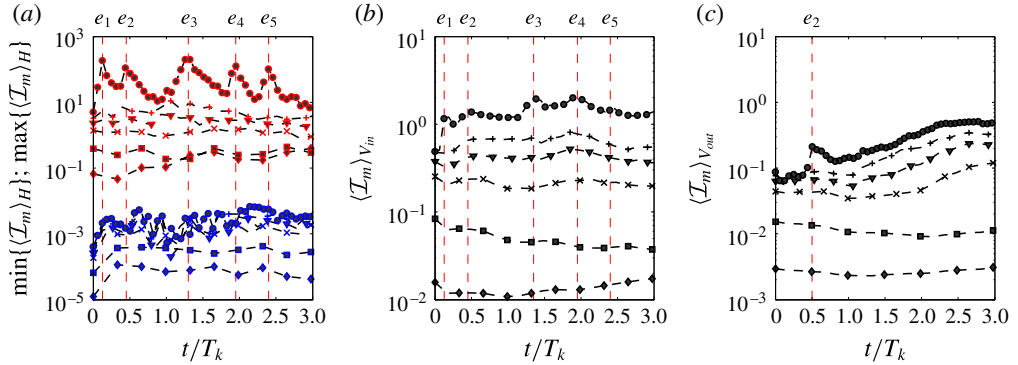
FIGURE 7. Evolution in time (scaled by T_K) of (*a*) the maximal and minimal values of the turbulence intensity parameter, (*b*) the bulk turbulence intensity parameter within R_i, $\langle\mathcal{I}_m\rangle_{V_{in}}$, and (*c*) the bulk turbulence intensity parameter outside R_i, $\langle\mathcal{I}_m\rangle_{V_{out}}$. Legend: $-\bullet-$, exp. 6; $-+-$, exp. 5; $-\blacktriangledown-$, exp. 4; $-\times-$, exp. 3; $-\blacksquare-$, exp. 2; $-\blacklozenge-$, exp. 1.

(e_i) with high turbulent activity (local maxima) in the time series of experiment 6 ($-\bullet-$), whose horizontal positions can be identified in figure 5(*b,d,g,i,j*). In figure 7(*a*) the values of min{$\mathcal{I}_m$} are comparable for all experiments except experiments 1 and 2 (blue lines), with min{$\mathcal{I}_m$} $\sim O(10^3)$. Values of max{$\mathcal{I}_m$}, however, increase with increasing nonlinearity, causing the separation of the time series between $O(10^{-1}) \leqslant$ max{$\mathcal{I}_m$} $\leqslant O(10^2)$ (red lines). In the case of experiment 6, peak turbulence intensity values are $O(10^5)$ times the background laminar value. These results show a significant heterogeneity of $\mathcal{I}_m$ in both time and space. We have divided the domain into two volumes: V_{in} and V_{out} denote the volumes within and outside R_i, respectively, and over these volumes bulk quantities of $\mathcal{I}_m$ have been calculated. Within R_i (see figure 7*b*), time series of $\langle\mathcal{I}_m\rangle_{V_{in}}$ show distinct differences between each experiments. The highest values and the most interesting temporal fluctuations are observed in experiment 6 ($-\bullet-$). Outside R_i (see figure 7*c*), time series show that $\langle\mathcal{I}_m\rangle_{V_{out}}$ tends to grow as a function of time, and shows only one peak at e_2 attributed to the formation of the first turbulent patch; figure 5(*d*) shows that this event (e_2) affects a small region outside R_i. Comparing both volumes, early in time, the distinction between the turbulent activity within and outside R_i is quite important, but by the later times in the experiments, $\mathcal{I}_m$ is only about a factor of 3 higher (see figure 7*b,c* for the most energetic case) and the tendency is to reduce the difference between both regions.

4.2. *Turbulence intensity and effective diffusivity*

Figures 8(*a*) and 8(*b*) show time series of the bulk averages of the turbulence intensity parameter, $\langle\mathcal{I}_m\rangle_V$, and the diffusivity parameter, $\langle\mathcal{K}_m\rangle_V$, respectively.

The temporal structure of $\langle\mathcal{I}_m\rangle_V$ (see figure 8*a*) is forced by the turbulent activity in the near-shore region (see peaks denoted by vertical dashed lines) but with lower magnitudes because of the low turbulent activity on the offshore region. Meanwhile, the time series of $\langle\mathcal{K}_m\rangle_V$ can be clustered into three groups (see figure 8*b*): a first group with experiments 1–3, a second group with experiments 4–5 and a third group with experiment 6. The first group contains experiments with the lowest and almost constant value of $\langle\mathcal{K}_m\rangle_V$, the second includes experiments with weak fluctuations of $\langle\mathcal{K}_m\rangle_V$, and the third group has the highest values and the strongest fluctuations of $\langle\mathcal{K}_m\rangle_V$. Experiment 6 is unique in that it yields substantially increased values of $\langle\mathcal{K}_m\rangle_V$
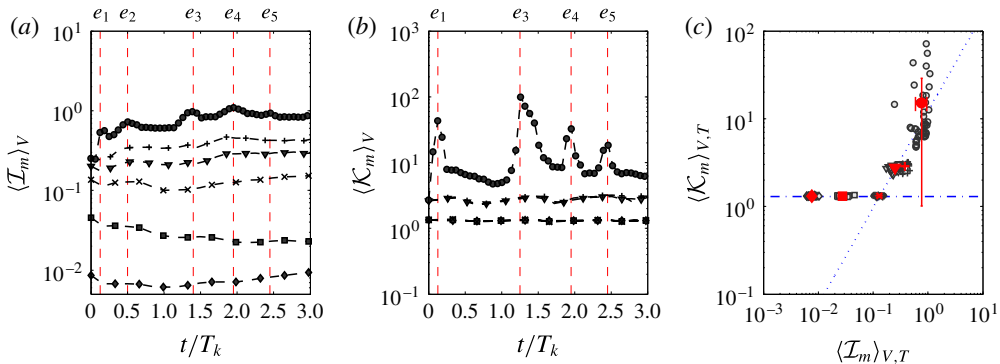
FIGURE 8. Evolution in time (scaled by T_K) of (a) the bulk turbulence intensity parameter, $\langle \mathcal{I}_m \rangle_V$, and (b) the bulk diffusivity parameter, $\langle \mathcal{K}_m \rangle_V$. Panel (c) exhibits $\langle \mathcal{K}_m \rangle_{V,T}$ versus $\langle \mathcal{I}_m \rangle_{V,T}$. Legend: –●–, exp. 6; –+–, exp. 5; –▼–, exp. 4; –×–, exp. 3; –■–, exp. 2; –◆–, exp. 1.

that are clearly correlated with individual breaking events (–●– and vertical dashed line in figure 8b). The temporal structure of $\langle \mathcal{K}_m \rangle_V$ indicates that episodic increases of the bulk diffusivity parameter are not directly correlated with the bulk-averaged turbulence intensity.

Figure 8(c) shows the volumetric and temporal averages, $\langle \cdot \rangle_{V,T}$, of $\mathcal{I}_m$ and $\mathcal{K}_m$. Red symbols correspond to $\langle \mathcal{K}_m \rangle_{V,T}$ against $\langle \mathcal{I}_m \rangle_{V,T}$ while the clusters of symbols around each red symbol correspond to $\langle \mathcal{K}_m \rangle_V(t)$ against $\langle \mathcal{I}_m \rangle_V(t)$ (data shown in figure 8a,b). Further, the standard deviations (s.d.) of the bulk values $\langle \cdot \rangle_V$ over time are shown (bars in the red symbols). We only see significant temporal variability in experiment 6, shown by –●– in figure 8(b) and the cluster of circles in figure 8(c). The large deviations seen in experiment 6 are a consequence of having approximately steady values of turbulence intensity (see figure 8a) but with very episodic elevated mixing (see figure 8b), suggesting that an instantaneous and local sampling of dissipation can be very misleading in terms of predicting the instantaneous mixing rate. On the other hand, averaging over all the events we identify a simple relation between $\langle \mathcal{K}_m \rangle_{V,T}$ and $\langle \mathcal{I}_m \rangle_{V,T}$. For values of $O(10^{-2}) \leqslant \langle \mathcal{I}_m \rangle_{V,T} \leqslant O(10^{-1})$ we find that $\langle \mathcal{K}_m \rangle_{V,T} \sim O(10^0)$, i.e. that the total diffusivity is not substantially elevated over that expected by laminar diffusion. For $O(10^{-1}) \leqslant \langle \mathcal{I}_m \rangle_{V,T} \leqslant O(10^1)$, however, the observed diffusivity is greater than that expected in a laminar flow and increases approximately linearly with turbulence intensity. The data fit a power law $\langle \mathcal{K}_m \rangle_{V,T} \sim a\{\langle \mathcal{I}_m \rangle_{V,T}\}^b$, with parameters $a = 12.2$ and $b = 1.1$. In the next subsection we describe the Kelvin wave evolution in the near-shore region and analyse the vertical distribution of $\mathcal{I}_m$ during the events e_2 and e_3.

4.3. *Flow evolution in the near-shore region*

Figure 9 shows a summary of the vertical stratification in experiment 6, $\mathcal{N}^2/\mathcal{N}_0^2$ (where $\mathcal{N}_0^2 \equiv \max\{\mathcal{N}^2(t=0)\}$), in the area $\mathcal{A}_\theta$ defined by $z/H \in [0, 1]$, $\theta \in [0, 2\pi]$ and $r/R = 0.98$, for 12 different times $t/T_k \in [0, 3]$. The region $\mathcal{A}_\theta$ allows us to observe the IKW evolution near the boundary where the wave displacements are maximal and where the maximal values of the turbulent activity are observed (see figure 5). Figure 9(b) shows KH-type instabilities in the early stages of the experiment ($t/T_k \approx 0.128$) because of the strong initial shear near the crest of the
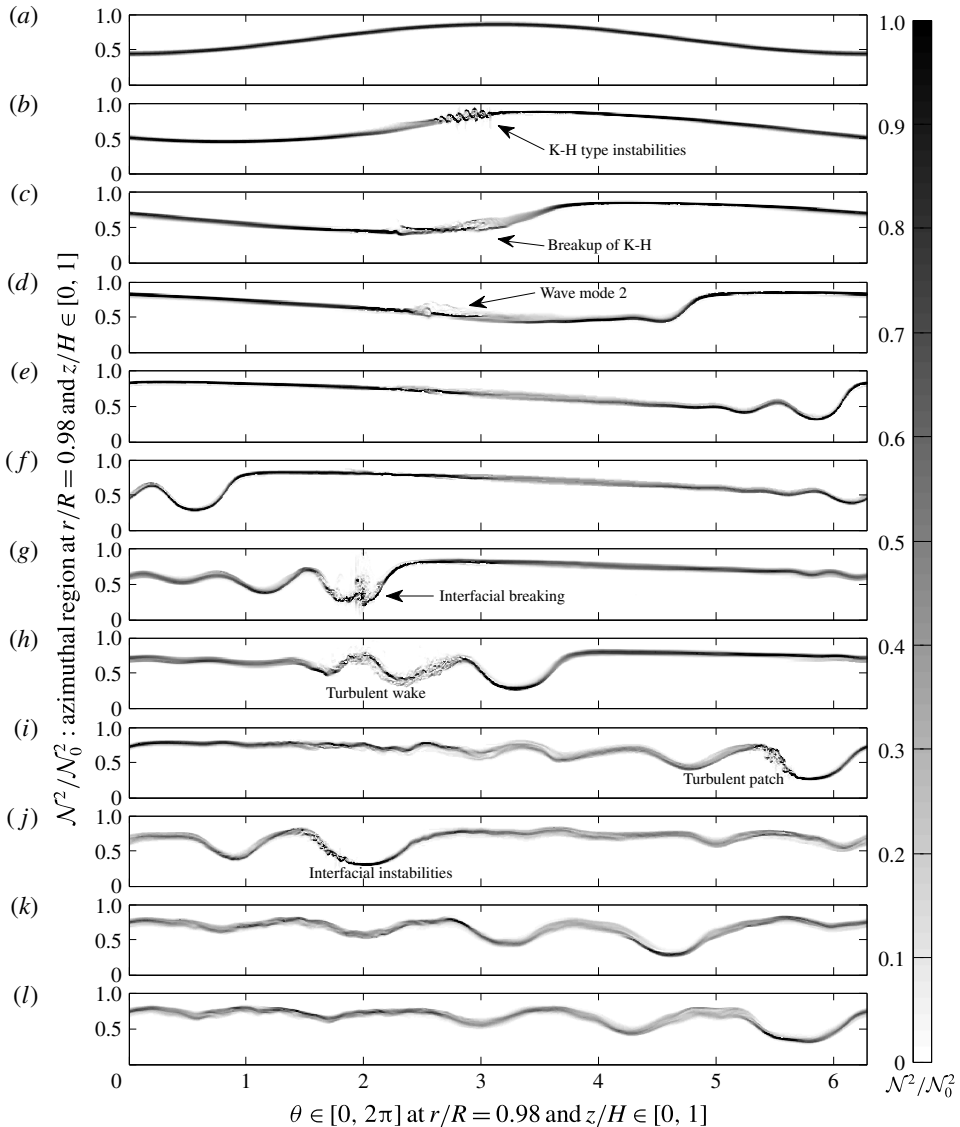
FIGURE 9. Results of experiment 6: evolution in time $t/T_k \in [0, 3]$ of the stratification, $\mathcal{N}^2/\mathcal{N}_0^2$, in the area $\theta \in [0, 2\pi]$, $z/H \in [0, 1]$ at $r/R = 0.98$. (a) $t/T_k = 0$, (b) $t/T_k = 0.128$, (c) $t/T_k = 0.25$, (d) $t/T_k = 0.5$, (e) $t/T_k = 0.75$, (f) $t/T_k = 1.0$, (g) $t/T_k = 1.128$, (h) $t/T_k = 1.5$, (i) $t/T_k = 2.0$, (j) $t/T_k = 2.25$, (k) $t/T_k = 2.75$, (l) $t/T_k = 3.0$.

IKW. Figure 9(c) shows the collapse or breakdown of the shear instabilities at $t/T_k \approx 0.25$. This process induces the formation of a turbulent patch and a local thickening of the density interface region that propagates along the shore region (see figures 9d and 5c). Simultaneously, the IKW has begun to steepen and form a solitary wave train (see figure 9d–f). After the first period, the leading wave of the solitary wave train interacts with the pre-existing stirred region (see figure 9g). The interaction generates interfacial breaking near the trough of the leading wave and a turbulent patch that subsequently spreads along the shore, over the solitary wave train (see figure 9g,h). This sequence of events is also observed after the second period (see
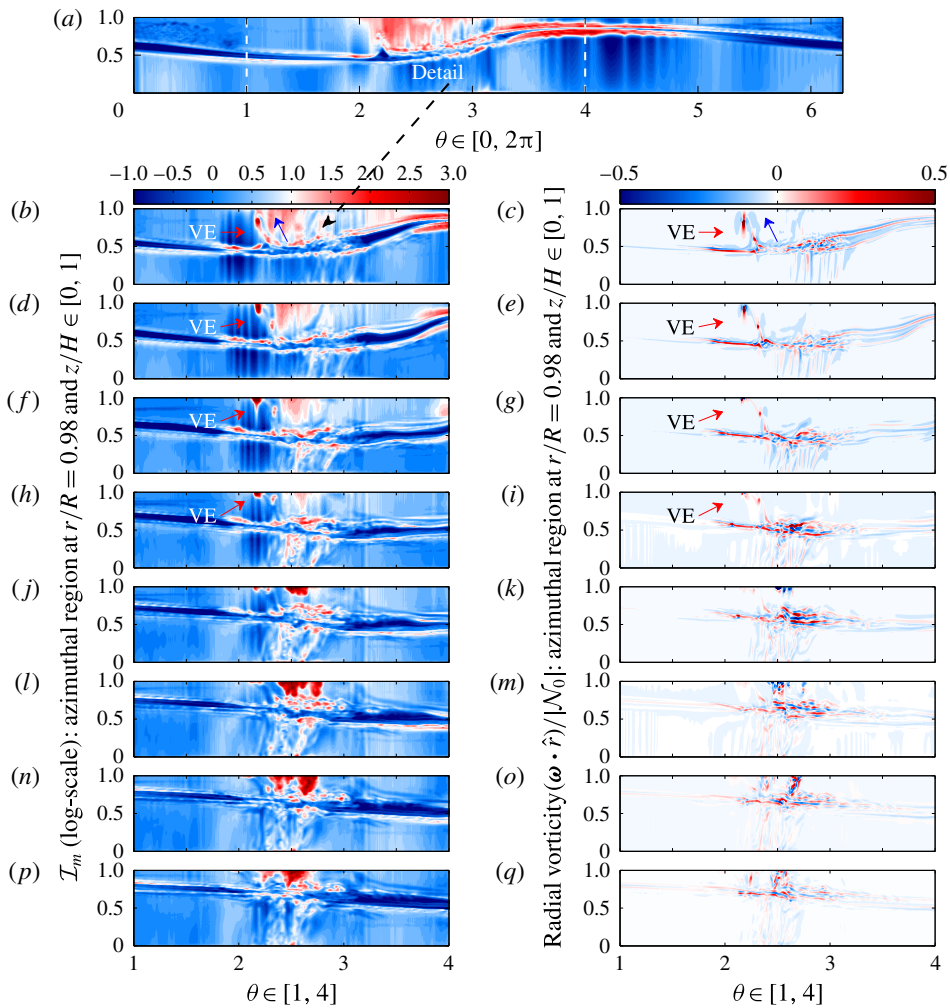
FIGURE 10. Results of experiment 6: evolution in time $t/T_k \in [0.25, 0.75]$ of the turbulence intensity parameter (in log scale) and radial vorticity in the region $\theta \in [0, \pi]$, $z/H \in [0, 1]$ at $r/R = 0.98$, during the peak of $\langle \mathcal{I}_m \rangle_V$, denoted by e_2 in figures 5(d), 7 and 8. (a) $t/T_k = 0.25$, (b,c) $t/T_k = 0.31$, (d,e) $t/T_k = 0.38$, (f,g) $t/T_k = 0.44$, (h,i) $t/T_k = 0.50$, (j,k) $t/T_k = 0.56$, (l,m) $t/T_k = 0.63$, (n,o) $t/T_k = 0.69$, (p,q) $t/T_k = 0.75$. VE: vortex ejection.

figure 9j), where interfacial instabilities on the trough and tail of the leading wave can be seen. After $t/T_k \approx 3$, the initial IKW has evolved into a solitary wave train that covers the area $\mathcal{A}_\theta$ and a significant thickening and weakening of the density interface as a consequence of vertical mixing is observed (see figure 9k,l).

4.3.1. *Turbulent patch and detrainment of vortices*

Figure 10 shows the turbulence intensity parameter, $\mathcal{I}_m$, and the radial vorticity scaled by the initial maximum buoyancy frequency, $(\boldsymbol{\omega} \cdot \hat{r}/|\mathcal{N}_0|)$, in the region $\mathcal{A}_\theta$, within the window time $t/T_k \in [0.25, 0.75]$. During this time the first two peaks of $\langle \mathcal{I}_m \rangle_V$ are registered (see figure 7(a), ϵ_1–ϵ_2). Figure 10(a) shows the turbulent activity during the breakdown of KH-type billows around $t/T_k \approx 0.25$. The maximum magnitudes of $\mathcal{I}_m$ ($\sim 10^1$–10^2) are identified in the density interface and the upper
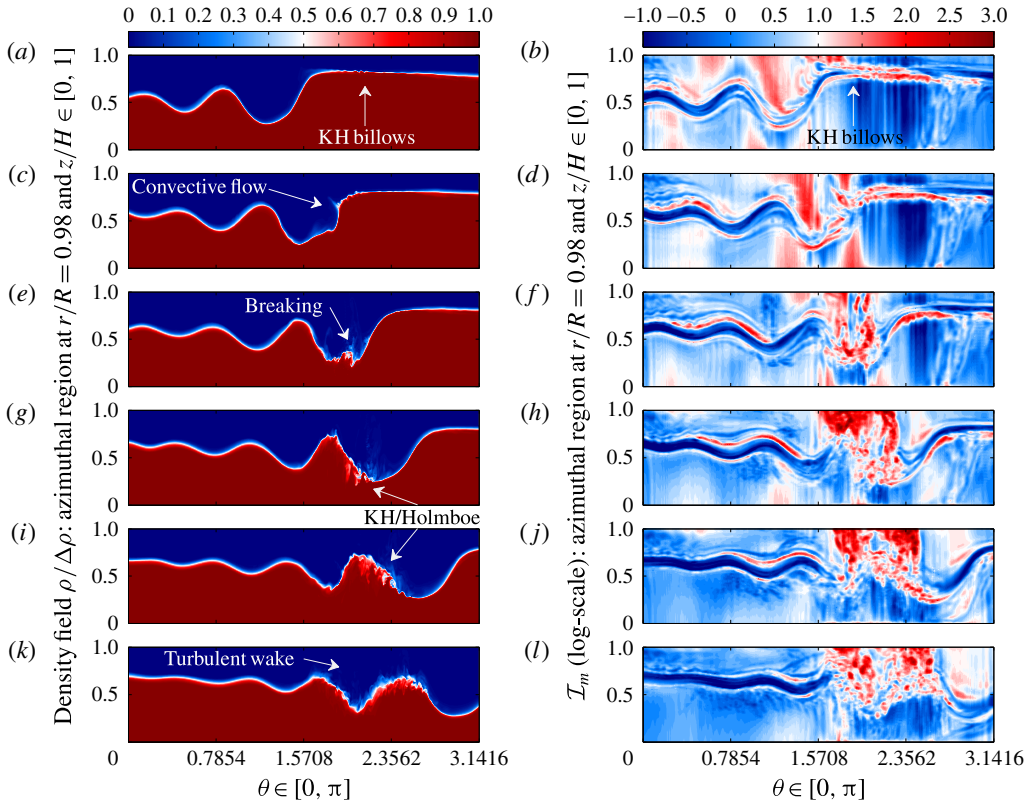
FIGURE 11. Results of experiment 6: evolution in time $t/T_k \in [1.12, 1.44]$ of the density field and turbulence intensity parameter during the breaking wave process in the region $\theta \in [0, \pi]$, $z/H \in [0, 1]$ at $r/R = 0.98$. (a,b) $t/T_k = 1.12$, (c,d) $t/T_k = 1.19$, (e,f) $t/T_k = 1.25$, (g,h) $t/T_k = 1.31$, (i,j) $t/T_k = 1.38$, (k,l) $t/T_k = 1.44$.

layer, near the crest and over the wavefront. We identify high-intensity spots of $\mathcal{I}_m$ (in red) that are ejected from the interfacial turbulent patch towards the top layer (blue arrow in figure 10a). Figure 10(b,d,f,h) illustrates the evolution (red arrows) of two red spots with $10^2 \leqslant \mathcal{I}_m \leqslant 10^3$. The radial vorticity field (see figure 10c,e,g,i) shows that these spots correspond to a coherent pair of counter-rotating vortices escaping from the interface region (blue arrow in figure 10c) by their mutual interaction, carrying small-scale turbulent fluid within their circulating cores into the ambient, non-turbulent water, thus enhancing the turbulent activity in the top layer (see figures 10j,l,n,p and 10k,m,o,q). This process is correlated with a local peak of the bulk turbulence intensity (event e_2 in figure 8a), but not with a local peak of the effective diffusivity parameter (see figure 8b). In this event, most of the higher spots of turbulence intensity are located near the top boundary, not in the mixing interface; therefore we expect a weaker response of the effective diffusivity parameter.

4.3.2. *Interfacial breaking and turbulent wake*

Figure 11 shows the density field and the turbulence intensity during the highest peaks of the turbulence activity parameters observed in experiment 6 (see events e_3 in figure 8a,b). During this time interval the solitary-type waves encounter and interact
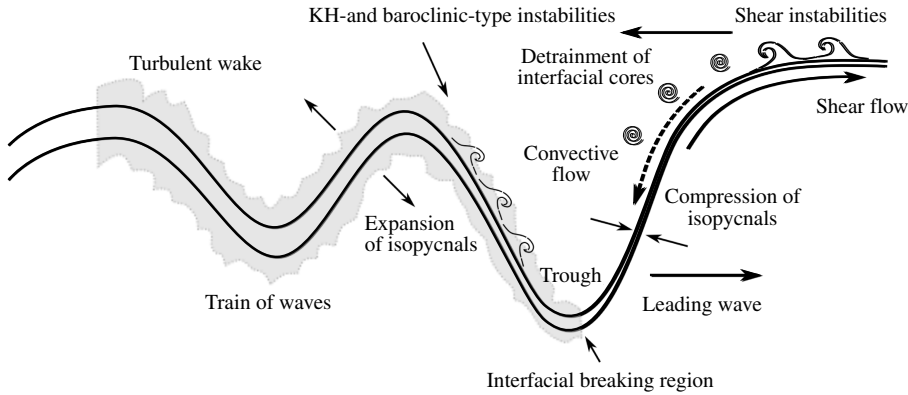
FIGURE 12. Schematic of the breaking wave process.

with the pre-existing turbulent patch shown in figure 10. The leading solitary-type wave induces a compression of the isopycnals in the density interface, increasing the buoyancy effects in the wavefront $\mathcal{N}^2 \sim |\partial_z \rho|$, but also enhancing the shear and the turbulent activity, $\epsilon_m \sim |\partial_z^m U|^2$, on the flat density region, upstream of the leading wave, from where interfacial instabilities start to re-emerge (see figure 11*a*,*b*). As the leading solitary wave crosses the sheared region, cores of interfacial fluid are ejected and transported through the top layer flow (see figure 11*c*,*d*). These processes induce local convection, which in turn enhances the turbulent activity on the internal face of the leading wave. Figure 11(*e*,*f*) shows a strong interfacial breaking on the trough of the leading wave. The interaction between this new source of turbulence and the solitary wave train induces an interfacial turbulent wake that is spread over the wave train. The turbulent wake is characterized by the growth and collapse of Kelvin–Helmholtz-type billows that lead to local unstable density conditions, which in turn trigger baroclinic-type instabilities by free convection (Matsumoto & Hoshino 2004; van Haren 2015) (see figure 11*g*–*l*). The wave breaking process and the subsequent turbulent wake is schematized in 12; similar schematics have been previously introduced by Moum *et al.* (2003) and Carr *et al.* (2008). The results suggest that the coupling of shear and convective flows plays an important role in the emergence of interfacial instabilities and breaking in steepened wavefronts (Preusse *et al.* 2012*a*,*b*).

5. Summary and discussion

Direct numerical simulations of the Boussinesq equations with a hyper-viscosity/ diffusivity (H-VD) approach have been conducted to examine the transition from a laminar to a turbulent regime in a flow induced by the gravest IKW in a continuous two-layer cylindrical domain at laboratory scale.

A range of values of the steepening parameter $\mathcal{T}_{sk}$, the damping parameter $\mathcal{T}_{vk}$ and the Richardson number $\mathcal{J}$, all related to the initial wave amplitude η_0, have been explored for a single Burger number $\mathcal{B}_i = 0.25$. Under this rotating regime, the IKW structure is strongly confined to the shore (Stocker & Imberger 2003). The results show the existence of four dynamic regimes and two regimes of turbulent activity.

The first three dynamic regimes have been analysed in previous numerical studies (de la Fuente *et al.* 2008; Sakai & Redekopp 2010), here called damped linear (DLR), nonlinear (NLR) and non-hydrostatic (NHR) regimes. These three regimes can also

Exp.	$\mathcal{T}_{vk}/\mathcal{T}_{sk}$	$\min\limits_{z\sim z_i}\{\mathcal{J}_0\}$	DLR	NLR	NHR	TR	i.i.[a]	i.b.[b]	$\langle\mathcal{I}_m\rangle_V$	$\langle\mathcal{K}_m\rangle_V$
1	3×10^{-3}	31.86	✓	×	×	×	0	0	$O(10^{-3}\text{–}10^{-2})$	$O(10^0)$
2	2×10^0	3.04	✓	✓	×	×	0	0	$O(10^{-2}\text{–}10^{-1})$	$O(10^0)$
3	4×10^2	0.58	✓	✓	✓	×	0	0	$O(10^{-1})$	$O(10^0)$
4	2×10^3	0.30	✓	✓	✓	×	0	0	$O(10^{-1}\text{–}10^0)$	$O(10^0\text{–}10^1)$
5	5×10^3	0.19	✓	✓	✓	✓	2	0	$O(10^{-1}\text{–}10^0)$	$O(10^0\text{–}10^1)$
6	10^4	0.13	✓	✓	✓	✓	4	1	$O(10^0\text{–}10^1)$	$O(10^1\text{–}10^2)$

TABLE 3. Regimes observed in the IKW evolution.

[a]Number of interfacial instabilities observed.
[b]Number of interfacial breaking observed.

be identified in laboratory experiments conducted by Ulloa *et al.* (2014), which studied the evolution of internal wavefields composed by rotating, basin-scale IGW. In particular, for similar dimensionless numbers, numerical and experimental results show clear similarity (e.g. compare figure 5*a* in Ulloa *et al.* (2014) with figure 2(*k*) of this paper). However, despite the similarities, our numerical results cannot be directly contrasted with those laboratory results because they substantially differ in the initial and boundary conditions. In the laboratory experiments the flow was induced by linear tilting of the density interface, and energy damping was governed by wall-friction. Here we present a fourth regime called the laminar–turbulent transition regime (TR). The TR is characterized by the growth of interfacial instabilities and the formation of turbulent patches as a consequence of the IKW degeneration. Observation of the TR motivates the analysis of the turbulent activity involved in the IKW evolution.

The first regime of the turbulent activity is related to the linear and weakly nonlinear dynamics of the IKW. Increasing η_0 to transition from the LR to the weakly nonlinear NHR produces only a moderate increase of the low values of the bulk turbulence intensity parameter $\langle\mathcal{I}_m\rangle_V$. It does not, however, significantly increase the overall rate of fluid mixing measured by the bulk effective diffusivity parameter $\langle\mathcal{K}_m\rangle_V$ (see the results of experiments 1–3 in figure 8). In this regime the sheared flow induced by the IKW and its weakly nonlinear degeneration is fully suppressed by the buoyancy, thus avoiding the transition from laminar to turbulent flow. The second regime of turbulent activity is related to the strong nonlinear dynamics of the IKW. The results show a substantial increase in turbulent activity as the flow evolves from the strong NHR to the TR (see the results of experiments 4–6 in figure 8). The strong degeneration of the IKW and the intensification of the shear flow in the wavefront of the leading wave destroy locally and intermittently the interface stability within the Rossby radius from the boundary, triggering the formation of intermittent turbulent patches from the growth and breakdown of Kelvin–Helmholtz-type billows. On the other hand, buoyancy imposes stability in the interior regions, though the turbulent activity there tends to increase as a consequence of the inertial gravity wave radiation from the near-shore to the offshore region (see figures 4 and 5). In this second regime, the nonlinear degeneration of the IKW and the turbulent episodes observed in experiments 4–6 are directly correlated with increases in the turbulence activity parameter, showing a power dependence between $\langle\mathcal{I}_m\rangle_V$ and $\langle\mathcal{K}_m\rangle_V$ (see figure 8*c*). Table 3 summarizes the IKW regimes.

We have identified four sources of turbulence in the TR: (i) interfacial instabilities driven by shear flows, (ii) the transport of vorticity from the interfacial region

to well-mixed layers driven by the mutual interaction of vortex pairs (with opposite sign), (iii) interfacial breakings, associated with the interaction of convective and shear flows over steep solitary-type waves and (iv) baroclinic-type instabilities presumably supported by the combination of vortex-type motions and shear flow in the near-shore region. The analysis of the emergence of interfacial instabilities in internal solitary waves (ISWs) has been addressed mainly via numerical study in a two-layer fluid, in a two-dimensional channel (Barad & Fringer 2010; Carr, King & Dritschel 2011; Almgren, Camassa & Tiron 2012; Preusse *et al.* 2012*b*). The numerical experiments of Carr *et al.* (2011) and Almgren *et al.* (2012) have shown that the growth of Kelvin–Helmholtz-type billows near the trough and tail of ISW amplitude (compare figures 7 and 8 by Carr *et al.* (2011) and Almgren *et al.* (2012), respectively, with our figure 9*i*,*j*) is close to the thickness of the top layer, $\eta_0/h_1 \approx 1$. In addition, the propagation of shear instabilities can disturb the tail and interact with a solitary wave train, giving rise to a turbulent wake in the density interface region, as shown by Barad & Fringer (2010) (see their figures 3 and 4 and our figures 9*h* and 11*g*,*i*,*k*). Parts of these previous results have been supported by laboratory experiments (Grue *et al.* 1999, 2000). Moreover, recent laboratory results have shown that convective instabilities in ISWs due to small-scale overturns may aid shear-induced instabilities on the wavefront (Carr *et al.* 2008; Fructus *et al.* 2009), giving feedback to the unstable state of the flow and enhancing the turbulence and mixing in the wave vicinity. In this context, our numerical study extends the analysis to nonlinear internal waves in enclosed rotating water bodies, such as medium or large lakes.

Field studies in stratified medium or large lakes have identified important sources of turbulence in the density interface attributed to shear instabilities (Kelvin–Helmholtz-type billows) riding over the slope of IKWs (Lorke 2007; Preusse *et al.* 2010). Furthermore, density inversion and interfacial breakings at the trough of a solitary wave train of large amplitudes have also been associated with the nonlinear degeneration of basin-scale IKWs (Preusse *et al.* 2010, 2012*a*,*b*). Both nonlinear processes have been observed in the TR of experiment 6. However, the interaction between interfacial turbulent patches and steep internal waves has not been studied and detected in detail in stratified lakes. This process can be a periodic source of turbulence and mixing in stratified lakes. In addition, the results suggest that the turbulence intensity is linked to the internal Rossby radius, and its horizontal distribution could be driven by the behaviour of the vertical vorticity (mainly observed in the near-shore region) and radial vorticity (mainly generated in the density interface region by shear flow), both processes as a consequence of the evolution and degeneration of the IKW.

The classification of the 'dynamic regimes' can be adopted for further use, but it is important to note that the regimes were established for a particular configuration of stratification ($h_1/H = 0.35$) and rotation ($B_i = 0.25$) and, indeed, the conditions to achieve them (LR, NL, NHR, TR) can change in terms of h_1/H and B_i (see e.g. Horn *et al.* 2001; Boegman *et al.* 2005; Ulloa *et al.* 2014).

To analyse the effect of rotation in the spatial distribution of turbulence as a consequence of the IKW degeneration, further studies are required. However, if the rotating regime changes (e.g. due to seasonal variations), for example to higher Burger numbers (larger R_i), the radial velocity component plays a more active role in the IKW propagation and the IKW can store more available potential energy within R_i. Therefore, variations in the rotating regime could change both the thresholds of dynamics regimes and the spatial distribution of turbulence induced by the IKW evolution.

As in Thomson (1879) and Csanady (1967), our study adopts the simplest representation possible for a rotating, stratified lake: a cylindrical basin with uniform depth. Moreover, to highlight the processes that promote wave steepening, degeneration and instability, we have excluded the effects of bottom friction. Real lakes, of course, have irregular shapes, frictional bottom boundary layers and shoaling bathymetry. How these features influence and modify the wave dynamics discussed here are important practical issues (see e.g. Beletsky *et al.* 1997; Boegman *et al.* 2003; Sakai & Redekopp 2010) that warrant further work.

Acknowledgements

Appendix A. Derivation of the turbulence activity parameter

We can derive the equation of the kinetic energy budget by taking the scalar product of the velocity field $\boldsymbol{v}$ with the momentum equation (see (2.1)). Then

$$\partial_t \mathscr{E}_k + (\boldsymbol{v} \cdot \nabla)\mathscr{E}_k = -\frac{\boldsymbol{v}}{\rho_0} \cdot (\nabla p + \rho g \hat{\boldsymbol{k}}) + \nu_m \boldsymbol{v} \cdot \nabla^{2m}(\boldsymbol{v}), \tag{A 1}$$

where $\mathscr{E}_k \equiv (\boldsymbol{v} \cdot \boldsymbol{v})/2$ is the kinetic energy per mass unit. Rearranging terms, the local time rate of change of kinetic energy can be expressed as follows:

$$\partial_t \mathscr{E}_k = -\nabla \cdot \left\{ \boldsymbol{v} \left(\mathscr{E}_k + \frac{p}{\rho_0} \right) - \nu_m \nabla^{h-1}(\boldsymbol{v} \cdot \nabla^m \boldsymbol{v}) \right\} - \frac{\rho}{\rho_0} g w - \nu_m |\nabla^m \boldsymbol{v}|^2. \tag{A 2}$$

The first term of the right-hand side of (A 2) gives the rate change of the kinetic energy resulting from advection, pressure and hyper-viscous diffusion of energy, the second term gives the reversible rate of exchange with potential energy due to buoyancy flux, while the third term gives the irreversible rate of hyper-viscous kinetic energy dissipation. Averaging (A 2) over a closed volume V, we obtain the following kinetic energy budget:

$$\partial_t \langle \mathscr{E}_k \rangle_V = -\frac{1}{V} \int_V \left\{ g w \frac{\rho}{\rho_0} \right\} \mathrm{d}V - \frac{1}{V} \int_V \{ \nu_m |\nabla^m \boldsymbol{v}|^2 \} \, \mathrm{d}V. \tag{A 3}$$

We are interested in the second term of (A 3):

$$\epsilon_m = \nu_m |\nabla^m \boldsymbol{v}|^2. \tag{A 4}$$

From ϵ_m and ν_m, the hyper-viscous Kolmogorov length scale can be calculated using the same arguments that set the ordinary ($m = 1$) Kolmogorov scale, resulting in

$$\ell_K \equiv \left\{ \frac{\nu_m^3}{\epsilon_m} \right\}^{1/(6m-2)}. \tag{A 5}$$

This scale defines where viscous forces balance inertial forces and the cascade is ultimately dissipated. The activity parameter is fundamentally the ratio of the Ozmidov scale and the Kolmogorov scale. The Ozmidov scale depends on the kinetic energy dissipation and the buoyancy frequency, and it is defined as follows:

$$\ell_O \equiv \left\{ \frac{\epsilon_m}{\mathcal{N}^3} \right\}^{1/2}. \tag{A 6}$$

This is the buoyancy scale at which the buoyant forces balance the inertial forces. A turbulence activity parameter will be a ratio, to some power (p) for convenience, of these two scales, i.e. a measure of how much bandwidth there is in the flow between the Ozmidov scale and the Kolmogorov scale (Barry *et al.* 2001):

$$\mathcal{I}_{m,p} \equiv \left\{ \frac{\ell_O}{\ell_K} \right\}^p = \left\{ \frac{\epsilon_m}{\nu_m^3} \right\}^{p/(6m-2)} \left\{ \frac{\epsilon_m}{\mathcal{N}^3} \right\}^{p/2}. \tag{A 7}$$

In the viscous case ($m = 1$), the turbulence activity parameter has been defined using $p = 4/3$. Thus

$$\mathcal{I}_m \equiv \left\{ \frac{\ell_O}{\ell_K} \right\}^{4/3} = \frac{\epsilon}{\mathcal{N}^2 \nu}. \tag{A 8}$$

If we keep the power $p = 4/3$ for the hyper-viscous version of the turbulence intensity parameter, we obtain the following expression:

$$\mathcal{I}_m \equiv \frac{1}{\mathcal{N}^2} \left\{ \frac{(\epsilon_m)^m}{\nu_m} \right\}^{2/(3m-1)}. \tag{A 9}$$

Appendix B. Derivation of the diffusivity parameter

We are interested in estimating how the mass diffusivity changes as a consequence of the evolution of an IKW in a two-layer flow. For this we will study the scales associated with the fluid mixing due to the flow and molecular action. We can analyse the fluid mixing via the time rate of change of the background potential energy per mass unit, $\mathscr{E}_b = \rho g z_* / \rho_0$:

$$\partial_t \mathscr{E}_b = \frac{g}{\rho_0} \partial_t \{ z_*(\boldsymbol{x}, t) \rho(\boldsymbol{x}, t) \} = \frac{g}{\rho_0} \{ z_* \partial_t \rho + \rho \partial_t z_* \}, \tag{B 1}$$

where z_* is the reference height in the minimum potential energy state of a fluid parcel at position ($\boldsymbol{x}, t$) (Winters *et al.* 1995; Winters & D'Asaro 1996). From the mass transport equation (see (2.1)), we can obtain the term $\partial_t \rho$ and replace it in (B 1), yielding

$$\partial_t \mathscr{E}_b = -\frac{g}{\rho_0} z_* \{ \boldsymbol{\nabla}(\boldsymbol{v} \rho) - \kappa_m \nabla^{2m} \rho \} + \frac{g \rho}{\rho_0} \partial_t z_*. \tag{B 2}$$

Because the z_* vertical coordinate depends implicitly on the density distribution $\rho(\boldsymbol{x}, t)$, we can write

$$z_* \boldsymbol{\nabla} \rho = \boldsymbol{\nabla} \xi \quad \text{where } \xi = \int^\rho z_*(\hat{\rho}) \, \mathrm{d}\hat{\rho}, \tag{B 3}$$

noting that $\boldsymbol{\nabla} z_* = (\mathrm{d}z_*/\mathrm{d}\rho)\boldsymbol{\nabla}\rho$. Using (B 3) and rearranging terms, the background potential energy budget can be written as follows:

$$\partial_t \mathscr{E}_b = -\frac{g}{\rho_0} \boldsymbol{\nabla}\{\boldsymbol{v}\xi - \kappa_m \boldsymbol{\nabla}(z_* \nabla^{2m-1}\rho)\} - \frac{g}{\rho_0}\kappa_m \left(\frac{\mathrm{d}\rho}{\mathrm{d}z_*}\right)^{-1} |\nabla^m \rho|^2 + \frac{g\rho}{\rho_0}\frac{\partial z_*}{\partial t}. \tag{B 4}$$

Averaging $\partial_t \mathscr{E}_b$ over a closed volume V, the first and third terms of the right-hand side of (B 4) are zero due to the no-flux boundary conditions and the mathematical construction of z_*, respectively (Winters *et al.* 1995). Hence, the background potential energy budget in a closed domain is reduced to the following expression:

$$\partial_t \langle \mathscr{E}_b \rangle_V = \frac{1}{V} \int_V - \left\{ \frac{g}{\rho_0}\kappa_m \left(\frac{\mathrm{d}\rho}{\mathrm{d}z_*}\right)^{-1} |\nabla^m \rho|^2 \right\} \mathrm{d}V. \tag{B 5}$$

Notice that the background density gradient, $\mathrm{d}\rho/\mathrm{d}z_*$, is a negative or null quantity, therefore $-\mathrm{d}\rho/\mathrm{d}z_*$ is a null or positive quantity, and therefore $\partial_t \langle \mathscr{E}_b \rangle_V$ is always positive. The expression integrated in (B 5) corresponds to the diapycnal flux given our m operators, ϕ_{hd}, which can be expressed in terms of the 'buoyancy', b, writing the density as $\rho = \rho_0(1 - g^{-1}b)$:

$$\phi_{hd} = \kappa_m \frac{|\nabla^m b|^2}{\mathrm{d}b/\mathrm{d}z_*}. \tag{B 6}$$

When the flow is turbulent, the buoyancy field is stirred and filamented and the numerator greatly exceeds the denominator. If we move to the laminar limit and imagine that the fluid is not at all stirred or filamented, but rather exists in its minimum potential energy state, then we can define a reference laminar diffusive flux for comparison. We call this flux ϕ_*, where

$$\phi_* = \kappa_m \frac{|\mathrm{d}^m b/\mathrm{d}z_*^m|^2}{\mathrm{d}b/\mathrm{d}z_*}. \tag{B 7}$$

We can now define an 'enhancement' parameter, measuring the increase in diffusive flux, due to turbulent stirring and straining, relative to the laminar, diffusive flux in a fluid with the same background buoyancy profile that is not stirred or strained:

$$\mathcal{K}_m \equiv \frac{\phi_{hd}}{\phi_*} = \frac{|\nabla^m b|^2}{\left|\mathrm{d}^m b/\mathrm{d}z_*^m\right|^2}. \tag{B 8}$$

Note that this reduces to the Cox number when $m = 1$ and always represents a ratio of turbulent diffusive flux to laminar diffusive flux for the same collection of fluid parcels, i.e. for a fluid with the same buoyancy profile state.

REFERENCES

ABRAMOWITZ, M. & STEGUN, A. 1965 *Handbook of Mathematical Functions: With Formulas, Graphs, and Mathematical Tables.* Dover.

ALMGREN, A., CAMASSA, R. & TIRON, R. 2012 Shear instability of internal solitary waves in Euler fluids with thin pycnoclines. *J. Fluid Mech.* **710**, 324–361.

ANTENUCCI, J. & IMBERGER, J. 2001 Energetics of long internal gravity waves in large lakes. *Limnol. Oceanogr.* **46**, 1760–1773.

BARAD, M. F. & FRINGER, O. B. 2010 Simulations of shear instabilities in interfacial gravity waves. *J. Fluid Mech.* **644**, 61–95.

BARRY, M. E., IVEY, G. N., WINTERS, K. B. & IMBERGER, J. 2001 Measurements of diapycnal diffusivities in stratified fluids. *J. Fluid Mech.* **442**, 267–291.

BELETSKY, D., O'CONNOR, W. P., SCHWAB, D. J. & DIETRICH, D. E. 1997 Numerical simulation of internal Kelvin waves and coastal upwelling fronts. *J. Phys. Oceanogr.* **27**, 1197–1215.

BOEGMAN, L., IMBERGER, J., IVEY, G. & ANTENUCCI, J. 2003 High-frequency internal waves in large stratified lakes. *Limnol. Oceanogr.* **48** (2), 895–919.

BOEGMAN, L., IVEY, G. & IMBERGER, J. 2005 The energetics of large-scale internal wave degeneration in lakes. *J. Fluid Mech.* **531**, 159–180.

BOEHRER, B. & SCHULTZE, M. 2008 Stratification of lakes. *Rev. Geophys.* **46**, RG2005.

BOUFFARD, D. & LEMMIN, U. 2013 Kelvin waves in Lake Geneva. *J. Great Lakes Res.* **39** (4), 637–645.

CARR, M., FRUCTUS, D., GRUE, J., JENSEN, A. & DAVIES, P. A. 2008 Convectively induced shear instability in large amplitude internal solitary waves. *Phys. Fluids* **20**, 126601.

CARR, M., KING, ST. E. & DRITSCHEL, D. G. 2011 Numerical simulation of shear-induced instabilities in internal solitary waves. *J. Fluid Mech.* **683**, 263–288.

CSANADY, G. T. 1967 Large-scale motion in the Great Lakes. *J. Geophys. Res.* **72**, 4151–4162.

CSANADY, G. T. 1981 On the structure of transient upwelling events. *J. Phys. Oceanogr.* **12**, 84–96.

FEDOROV, A. & MELVILLE, W. K. 1995 Propagation and breaking of nonlinear Kelvin waves. *J. Phys. Oceanogr.* **25**, 2518–2531.

FLÓR, J.-B., SCOLAN, H. & GULA, J. 2011 Frontal instabilities and waves in a differentially rotating fluid. *J. Fluid Mech.* **685**, 532–542.

FRUCTUS, D., CARR, M., GRUE, J., JENSEN, A. & DAVIES, P. A. 2009 Shear-induced breaking of large internal solitary waves. *J. Fluid Mech.* **620**, 1–29.

DE LA FUENTE, A., SHIMIZU, K., IMBERGER, J. & NIÑO, Y. 2008 The evolution of internal waves in a rotating, stratified, circular basin and the influence of weakly nonlinear and nonhydrostatic accelerations. *Limnol. Oceanogr.* **53** (6), 2738–2748.

DE LA FUENTE, A., SHIMIZU, K., NIÑO, Y. & IMBERGER, J. 2010 Nonlinear and weakly nonhydrostatic inviscid evolution of internal gravitational basin-scale waves in a large, deep lake: Lake Constance. *J. Geophys. Res.* **115**, C12045.

GRIMSHAW, R. H. J. 1985 Evolution equation for weakly nonlinear, long internal waves in a rotating fluid. *Stud. Appl. Maths* **73**, 1–33.

GRUE, J., JENSEN, A., RUSAS, P.-O. & SVEEN, J. K. 1999 Properties of large-amplitude internal waves. *J. Fluid Mech.* **380**, 257–278.

GRUE, J., JENSEN, A., RUSAS, P.-O. & SVEEN, J. K. 2000 Breaking and broadening of internal solitary waves. *J. Fluid Mech.* **413**, 181–217.

GULA, J., PLOUGONVEN, R. & ZEITLIN, V. 2009 Ageostrophic instabilities of fronts in a channel in a stratified rotating fluid. *J. Fluid Mech.* **627**, 485–507.

VAN HAREN, H. 2015 Instability observations associated with wave breaking in the stable-stratified deep-ocean. *Physica* D **292–293**, 62–69.

HELFRICH, K. & MELVILLE, W. K. 2006 Long nonlinear internal waves. *Annu. Rev. Fluid Mech.* **38**, 395–425.

HORN, D. A., IMBERGER, J. & IVEY, G. N. 2001 The degeneration of large-scale interfacial gravity waves in lakes. *J. Fluid Mech.* **434**, 181–207.

KUNDU, P. & COHEN, I. 2004 *Fluid Mechanics.* Elsevier Academic.

LAMB, H. 1932 *Hydrodynamics*, 6th edn. Dover.

LAMORGESE, A. G., CAUGHEY, D. A. & POPE, S. B. 2005 Direct numerical simulation of homogeneous turbulence with hyperviscosity. *Phys. Fluids* **17**, 015106.

LORKE, A. 2007 Boundary mixing in the thermocline of a large lake. *J. Geophys. Res.* **112**, C09019.

LORKE, A., PEETERS, F. & BÄUERLE, E. 2006 High-frequency internal waves in the littoral zone of large lake. *Limnol. Oceanogr.* **51** (4), 1935–1936.

MATSUMOTO, Y. & HOSHINO, M. 2004 Onset of turbulence induced by a Kelvin–Helmholtz vortex. *Geophys. Res. Lett.* **31**, L02807.

MILES, J. W. 1961 On the stability of heterogeneous shear flows. *J. Fluid Mech.* **10**, 496–508.

MOUM, J. N., FARMER, D. M., SMYTH, W. D., ARMI, L. & VAGLE, S. 2003 Structure and generation of turbulence at interfaces strained by internal solitary waves propagating shoreward over the continental shelf. *J. Phys. Oceanogr.* **33**, 2093–2112.

PEDLOSKY, J. 1970 Finite-amplitude baroclinic waves. *J. Atmos. Sci.* **27**, 15–30.

PEDLOSKY, J. 1987 *Geophysical Fluid Dynamics*. Springer.

PREUSSE, M., FREISTÜHLER, H. & PEETERS, F. 2012a Seasonal variation of solitary wave properties in Lake Constance. *J. Geophys. Res.* **117**, C04026.

PREUSSE, M., PEETERS, F. & LORKE, A. 2010 Internal waves and the generation of turbulence in the thermocline of a large lake. *Limnol. Oceanogr.* **55** (6), 2353–2365.

PREUSSE, M., STASTNA, M., FREISTÜHLER, H. & PEETERS, F. 2012b Intrinsic breaking of internal solitary waves in a deep lake. *PLoS ONE* **7**, e41674.

ROZAS, C., DE LA FUENTE, A., ULLOA, H., DAVIES, P. & NIÑO, Y. 2014 Quantifying the effect of wind on internal wave resonance in Lake Villarrica, Chile. *Environ. Fluid Mech.* **14** (4), 849–871.

SAKAI, S. 1989 Rossby–Kelvin instability: a new type of ageostrophic instability caused by a resonance between Rossby waves and gravity waves. *J. Fluid Mech.* **202**, 149–176.

SAKAI, T. & REDEKOPP, L. G. 2010 A weakly nonlinear evolution model for long internal waves in a large lake. *J. Fluid Mech.* **637**, 137–172.

SHIMIZU, K. & IMBERGER, J. 2009 Damping mechanisms of internal waves in continuously stratified rotating basins. *J. Fluid Mech.* **637**, 137–172.

SPYKSMA, K., MAGCALAS, M. & CAMPBELL, N. 2012 Quantifying effects of hyperviscosity on isotropic turbulence. *Phys. Fluids* **24**, 125102.

STOCKER, R. & IMBERGER, J. 2003 Energy partitioning and horizontal dispersion in a stratified rotating lake. *J. Phys. Oceanogr.* **33**, 512–529.

THOMSON, W. (LORD KELVIN) 1879 On gravitational oscillations of rotating water. *Proc. R. Soc. Edinburgh.* **10**, 92–100.

ULLOA, H. N., DE LA FUENTE, A. & NIÑO, Y. 2014 An experimental study of the free evolution of rotating, nonlinear internal gravity waves in a two-layer stratified fluid. *J. Fluid Mech.* **742**, 308–339.

WAITE, M. L. & BARTELLO, P. 2004 Stratified turbulence dominated by vortical motion. *J. Fluid Mech.* **517**, 281–308.

WAKE, G. W., IVEY, G. N. & IMBERGER, J. 2005 The temporal evolution of baroclinic basin-scale waves in a rotating circular basin. *J. Fluid Mech.* **523**, 367–392.

WINTERS, K. B. & D'ASARO, E. A. 1996 Diascalar flux and the rate of fluid mixing. *J. Fluid Mech.* **317**, 179–193.

WINTERS, K. B. & D'ASARO, E. A. 1997 Direct simulation of internal wave energy transfer. *J. Phys. Oceanogr.* **27**, 1937–1945.

WINTERS, K. B. & DE LA FUENTE, A. 2012 Modelling rotating stratified flows at laboratory-scale using spectrally-based DNS. *Ocean Model.* **50**, 47–59.

WINTERS, K. B., LOMBARD, P. N., RILEY, J. J. & D'ASARO, E. A. 1995 Available potential energy and mixing in density-stratified fluids. *J. Fluid Mech.* **289**, 115–128.

WÜEST, A. & LORKE, A. 2003 Small-scale hydrodynamics in lakes. *Annu. Rev. Fluid Mech.* **35**, 373–412.